

ABSTRACT

Title of thesis: Flowfield Estimation and Vortex
Stabilization near an Actuated Airfoil

Daniel Fernando Gomez Berdugo
Master of Science, 2019

Thesis directed by: Professor Derek A. Paley
Department of Aerospace Engineering and
Institute for Systems Research

Feedback control of unsteady flow structures is a challenging problem that is of interest for the creation of agile bio-inspired micro aerial vehicles. This thesis presents two separate results in the estimation and control of unsteady flow structures: the application of a principled estimation method that generates full flowfield estimates using data obtained from a limited number of pressure sensors, and the analysis of a nonlinear control system consisting of a single vortex in a freestream near an actuated cylinder and an airfoil. The estimation method is based on Dynamic Mode Decompositions (DMD), a data-driven algorithm that approximates a time series of data as a sum of modes that evolve linearly. DMD is used here to create a linear system that approximates the flow dynamics and pressure sensor output from Particle Image Velocimetry (PIV) and pressure measurements of the flowfield around the airfoil. A DMD Kalman Filter (DMD-KF) uses the pressure measurements to estimate the evolution of this linear system, and thus produce an approximation of the flowfield from the pressure data alone. The DMD-KF is imple-

mented for experimental data from two different setups: a pitching cambered ellipse airfoil and a surging NACA 0012 airfoil. Filter performance is evaluated using the original flowfield PIV data, and compared with a DMD reconstruction. For control analysis, heaving and/or surging are used as input to stabilize the vortex position relative to the body. The closed-loop system utilizes a linear state-feedback control law. Conditions on the control gains to stabilize any of the equilibrium points are determined analytically for the cylinder case and numerically for the airfoil. Simulations of the open- and closed-loop systems illustrate the bifurcations that arise from varying the vortex strength, bound circulation and/or control gains.

Flowfield Estimation and Vortex Stabilization near an Actuated
Airfoil

by

Daniel Fernando Gomez

Thesis submitted to the Faculty of the Graduate School of the
University of Maryland, College Park in partial fulfillment
of the requirements for the degree of
Master of Science
2019

Advisory Committee:
Professor Derek A. Paley, Advisor
Professor Anya R. Jones
Professor Robert M. Sanner

© Copyright by
Daniel Fernando Gomez
2019

Dedication

I would like to dedicate this thesis to my family, who have supported me on every step of the way.

Acknowledgments

I want to thank my advisor Dr. Derek Paley for being a great mentor during these two years. Dr. Frank Lagor for helping me hit the ground running when beginning my graduate studies and continued support. Andrew Lind and Philip Kirk for letting me use their experimental data and thoroughly answering my questions. My labmates from the Collective Dynamics and Controls Lab, especially Travis Burch and Jordan Boehm for keeping check on one another during stressful times, Will Craig for being a great office mate, and Debdipta Goswami for incredibly interesting conversations. Girguis Sedky, Jonathan Lefebvre, Luke Smith, Hülya Bilder and André Bauknecht for answering my questions about unsteady aerodynamics and for welcoming me in many lab activities as an ‘honorary member’. Dr. Anya Jones for her valuable feedback, Dr. Robert Sanner for two great courses from which I learned immensely and both for being part of my committee. International Friends Club, Maryland Latin Dance Club, and Terrapin Trail Club for being like second families far from home. Without your help and support I would not have achieved as much in my work, nor enjoyed as much during my studies at University of Maryland.

Finally I want to thank the Clark School of Engineering for providing financial support through a Clark Doctoral Fellowship. This research was funded in part by AFOSR Grant No. FA95501810137.

Table of Contents

Dedication	ii
Acknowledgements	iii
List of Tables	vi
List of Figures	vii
List of Abbreviations	ix
1 Introduction	1
1.1 Motivation and Approach	1
1.1.1 Approach for Estimation	3
1.1.2 Approach for Control	5
1.2 Relation to Prior Work	5
1.2.1 Dynamic Mode Decomposition for Flowfield Analysis	5
1.2.2 Control of Vortices near a Cylinder or Airfoil	6
1.3 Contributions of Thesis	7
1.4 Thesis Outline	8
2 Background	10
2.1 Potential Flow Modeling	10
2.1.1 Dynamics of a point vortex near a cylinder	11
2.1.2 Dynamics of a Point Vortex Near an Actuated Airfoil	12
2.1.2.1 Joukowski Transform	13
2.1.2.2 Kutta condition	13
2.1.2.3 Routh correction	14
2.2 Dynamic Mode Decomposition	17
2.2.1 Base algorithm	17
2.2.2 Sparsity Promoting Dynamic Mode Decomposition	20
2.2.3 Dynamic Mode Decomposition Kalman Filter	21
2.2.4 Sources of Error in the Dynamic Mode Decomposition Kalman Filter	24

2.2.5	More concepts in DMD	26
3	Data Driven Estimation of Unsteady Flowfield near an Actuated Airfoil	27
3.1	Dynamic Mode Decomposition on an Actuated Airfoil	27
3.2	Dynamic Mode Decomposition Kalman Filter estimation results	32
3.2.1	Experiment 1: Pitching cambered ellipse	33
3.2.2	Experiment 2: Surging NACA 0012	37
3.3	Summary	40
4	State Feedback Stabilization of a Point Vortex near an actuated Airfoil	42
4.1	Dynamics of a Point Vortex Near a Cylinder	42
4.1.1	Bifurcations of the Open-Loop Dynamics	43
4.1.2	Closed-Loop Dynamics and bifurcations	45
4.1.3	Summary of results for the cylinder-vortex system	54
4.2	Dynamics of a Point Vortex Near an Airfoil	54
4.2.1	Open-Loop Equilibrium points and dynamics	54
4.2.2	Closed-Loop Dynamics for a vortex near an airfoil	56
4.2.3	Summary of results for the airfoil-vortex system	57
5	Conclusion	58
5.1	Summary of Contributions	58
5.2	Suggestions for Ongoing and Future Work	59
	Bibliography	61

List of Tables

3.1	Summary of experimental parameters.	29
3.2	Actuation parameters for Experiment 2.	29

List of Figures

2.1	The drifting vortex is convected by the influence of the freestream, the cylinder, the image vortex, and the bound vortex.	11
2.2	Geometrical relation between terms of (2.7).	15
3.1	Configuration of Experiments 1 [45] and 2 [46]. Teal arrows indicate direction of actuation	28
3.2	Actuation trajectories for Experiment 2.	29
3.3	(a) Number of modes chosen by DMDSP for different values of γ ; (b, d) percent performance loss versus number of modes; (c) comparison of projection error for DMD and POD modes.	31
3.4	Training set data and reconstructions with different number of modes for Experiment 1 at half the actuation period ($t^*=0.5$).	32
3.5	Experiment 1: Estimation, reconstruction, and projection errors. The vertical lines in (e) correspond to the frames shown in Figure 3.6.	35
3.6	Experiment 1: Test set data, training set data, and estimate of the test data with 13 modes at several times of interest. The color red (blue) indicates positive (negative) vorticity.	36
3.7	Experiment 2: Estimation, reconstruction error and projection. The vertical lines in Case 3 indicate the frames shown in Figure 3.8. . . .	37
3.8	Experiment 2: Original and estimated flowfield and estimation error using 19 modes at several times of interest for case 3. For the error field, the color red indicates magnitude.	39
4.1	a) The black regions show the area in parameter space where the system has three equilibrium points. The dashed line corresponds to the slice shown in Figure 4.1b. b) Bifurcation diagram fixing $\sigma_v = 2$ and varying σ_0 . Equilibrium points far from the cylinder approach the line $\sigma_0 = \sigma_v$, shown as a dotted line.	45
4.2	Phase portraits for $\sigma_v = 2$. and (a) $\sigma_0 = 0$, (b) $\sigma_0 = 5.5$	46

4.3	Phase planes for the closed-loop system with $\sigma_v = 2, \sigma_0 = 0$, and non-zero cross gains k_{12} (a–b) or k_{21} (c–d). The red X indicates the original equilibrium point, the red dots indicate the new equilibrium points that appear due to feedback. (a) and (c) have gains below conditions (4.18) and (4.21), respectively. (b) and (d) have gains above condition (4.18) and (4.21), respectively.	51
4.4	Phase planes for the closed-loop with $\sigma_v = 2, \sigma_0 = 0$, and multiple two-gain designs that exponentially stabilize the equilibrium point. The red X indicates the original equilibrium point, the red dots indicate the saddles that appear due to feedback. The trajectories shown approximate the stable and unstable manifolds of the saddles.	53
4.5	Equilibrium points for a vortex near an airfoil in (a) [38] (b) airfoil plane, (c) cylinder plane.	55
4.6	Phase portrait for a vortex of strength $\Gamma_v = -5$ near an airfoil at an angle of attack of 10° in the a) airfoil plane b) circle plane. Arrows indicate only direction, not magnitude.	55
4.7	Phase portrait for a vortex of strength $\Gamma = -5$ near an airfoil at an angle of attack of 10° with closed loop control in the a) airfoil plane b) circle plane. Arrows indicate only direction, not magnitude.	57

List of Abbreviations

LEV	Leading Edge Vortex
MAV	Micro Aerial Vehicle
PIV	Particle Image Velocimetry
DMD	Dynamic Mode Decomposition
DMD-KF	Dynamic Mode Decomposition Kalman Filter
KOF	Koopman Observer Form

Chapter 1: Introduction

1.1 Motivation and Approach

Unsteady flow structures play an important role in the generation of lift in flow regimes with separated flow. Separated flow typically occurs in cases with low Reynolds numbers, high angles of attack, rapid airfoil motion, or in the presence of gusts [1]. These conditions are typical for small scale flyers such as insects, birds, and micro aerial vehicles (MAVs) [2]. The rise in popularity of MAVs has led to increased interest in modeling and control of unsteady separated flow. In fixed wing aircraft, unsteady flow structures are usually undesirable, but biological flyers such as insects and birds take advantage of flow structures to enhance lift or reject gusts [2].

As a motivating example, during dynamic stall, the lift coefficient increases beyond its value found in the static stall condition, due to the formation of a leading edge vortex (LEV). As the angle of attack increases further, the LEV sheds and the lift coefficient falls [3]. Some insects are able to stabilize the LEV to take advantage of the increased lift [4]. There is great interest in applying feedback control to enhance or regularize unsteady lift production by stabilizing the leading edge vortex.

Feedback control of an airfoil can be divided into two problems: (1) given a

set of measurements, determine what is the state of the flowfield and (2) given the state of the flowfield, determine what should be the actuation command in order to obtain the desired lift. These are referred as the estimation and the control problems respectively. Solving this feedback control problem fully is beyond the scope of this thesis. Instead, this work presents an approach to each of these problems separately and the results obtained therein.

A prerequisite for feedback control based on flow structures is a tractable model of the flowfield dynamics. Modeling of unsteady flow has been done since the early days of aerodynamics. However, such models take advantage of small angle or inviscid flow assumptions to develop an analytic solution and thus are not suitable in more general cases [1]. The flowfield near an airfoil is governed by nonlinear partial differential equations. Accurate solutions exist in the form of computational fluid dynamic solvers; however these are computationally expensive and the state space is usually intractable for the purpose of estimation and control. A simple mathematical model for the evolution of a LEV and the forces on the airfoil is still an open question. Current approaches focus on data-driven methods and potential flow models [2]. The approach in this thesis is to use a data driven modal decomposition approach for estimation and a simplified potential flow model for control.

1.1.1 Approach for Estimation

Estimation can be achieved by a dynamic observer operating on a model of the flowfield. Common approaches include linearization of the Navier-Stokes equations [5], fitting a reduced-order model to experimental data, such as the Goman-Khrabrov model [6], or using modal decompositions [7].

Modal decomposition methods extract a small number of modes that contain most of the information from a set of high-dimensional data. For example, Proper Orthogonal Decomposition (POD) [8] provides a set orthogonal modes that can be used to optimally represent the original dataset in an energetic (least-squares) sense. A reduced number of POD modes can be used to reproduce the original dataset; however, these modes do not necessarily correspond to structures that evolve coherently in time and space [9]. Balanced POD (BPOD) [10] finds modes that are the most controllable and observable, making it very useful for feedback control as in [11]. However, BPOD requires prior knowledge of the dynamics of the system [7].

An alternative modal decomposition that focuses on describing the time evolution of the states is Dynamic Mode Decomposition (DMD). DMD is a data-driven algorithm initially developed for modal decomposition and analysis of fluid flows [12]. In the context of fluid mechanics, DMD decomposes the flow into modes of oscillation and, thus, provides a useful dynamical description of the system. DMD has been commonly used to analyze the behavior of unsteady flow [7]. The traditional procedure used for analyzing a flow using DMD is to assimilate velocity data ob-

tained either computationally or through Particle Image Velocimetry (PIV). Modal decomposition generates a reduced-order, approximate model in terms of the DMD modes, which may be used for estimation.

If DMD is performed with both state and output data, a linear system that approximates the dynamics and the output equation can be constructed, and a Kalman Filter (KF) may be applied to estimate the states [13]. We refer to this filter as a DMD Kalman Filter (DMD-KF). This thesis applies the DMD-KF to generate full flowfield estimates using DMD modes and data obtained from a limited number of pressure sensors. Define the original data set as the training set, which contains PIV data and pressure measurements. Sparsity Promoting DMD (DMDSP) selects a reduced number of modes in order to simplify the system, while providing a sufficiently accurate approximation of the flowfield. The DMD-KF uses pressure measurements as inputs to estimate a linear dynamical system in which the states are the amplitudes of the DMD modes. With knowledge of the modes and an estimate of the amplitudes, the flowfield is reproduced. The performance of the estimator is evaluated with the original training data set and a separate test data set consisting of a different realization of the same system. Although our analysis was conducted offline, the estimator may be useful for real-time analysis and control of a flowfield when distributed pressure measurements are available, but in-situ PIV measurements are not.

1.1.2 Approach for Control

Most approaches to modeling the leading edge use a point vortex model. This model assumes inviscid flow with vorticity contained in point vortices. With enough point vortices, the model approximates the behavior of a continuous vorticity distribution. A point vortex model sheds point vortices to model the generation and shedding of vorticity from the leading and trailing edges of an airfoil. The aim of this work is the stabilization of a leading edge vortex (LEV), which forms and sheds off of airfoils at high angles of attack during dynamic maneuvers. The leading edge vortex presents itself as a large vortical structure above the airfoil that grows, sheds, and grows again [14]. Motion of the airfoil perpendicular and parallel to the freestream is called heaving and surging, respectively. We consider heaving and/or surging as control inputs to the LEV stabilization problem. This work presents a first step in developing a feedback control law that stabilizes a vortex near an airfoil. This thesis models the vortical structure as a single vortex, an approach that was considered in [15]. Initially we present the stabilization of a vortex near a cylinder. Then the model is extended to an airfoil.

1.2 Relation to Prior Work

1.2.1 Dynamic Mode Decomposition for Flowfield Analysis

The DMD-KF is different from [16] [17] in which the Kalman filter is used for obtaining the DMD modes more precisely in the presence of noise. To be useful for

estimation, the DMD modes should not only represent the dataset in which DMD was performed, but also the ensemble of flow trajectories possible for the underlying dynamics. Ideally, it is desirable to obtain modes that are physically significant to the system, instead of modes that fit patterns specific to the data used to compute DMD modes. Physically significant modes may more accurately represent different realizations of the same system. Indeed, DMD may be able to provide such a general model of the dynamics even if the system is nonlinear.

Obtaining physically significant modes is a goal of many DMD-related papers: Extended DMD [18] uses a dictionary of functions to better approximate the Koopman operator of the underlying dynamics; Total DMD [19] [20] seeks to correct for the effect of noisy data; [9] shows that Spectral POD optimally accounts for the variation in an ensemble of DMD modes; and Sparsity Promoting DMD (DMDSP) [21] finds the most relevant DMD modes for a set of data. Implementing these variations of DMD could potentially improve the performance of the DMD-KF, however such an exploration lies beyond the scope of this thesis. Other works have used DMD with pressure measurements to obtain optimal actuation frequencies for open-loop control [22], predicting forces on a pitching airfoil [23], and performing feedback control for flow reattachment [24].

1.2.2 Control of Vortices near a Cylinder or Airfoil

The interaction of vortices with other bodies, especially airfoils and wings has been extensively studied in the fluid dynamics literature. Approaches for vortex sta-

bilization often involve passive structures [25] and jets [26]. Rotational accelerations have been found to stabilize LEV on revolving wings [27]. Vortex-cylinder models have also been used extensively in recent years to model the vortex shedding of a swimming fish [28]. The simple potential flow, vortex-cylinder system considered in this work has been studied in [29], in which equilibrium point and bifurcations are analyzed. In [15] a control law is designed using simple vortex-cylinder model and tested with a simulation with Navier-Stokes equations. The new contribution presented here lies in a detailed analysis on the conditions on feedback gains that lead to stability and the corresponding bifurcations that arise from feedback.

1.3 Contributions of Thesis

This thesis can be split into two independent sections. The first is the description and implementation of a data-driven method for flow field estimation using pressure sensors near an actuated airfoil. The second is the stability analysis of two nonlinear systems: a vortex in the presence of an actuated cylinder and a vortex in the presence of an airfoil.

The main contribution of the estimation section is to apply the DMD-KF to experimental flowfield and pressure sensor data generated by actuated airfoils at high angles of attack, an unsteady condition of interest for the application of feedback control. The first experiment, a pitching cambered ellipse, illustrates the selection of modes for the reduced-order model and shows the effect of the number of modes on the performance of the estimator. The second experiment, a surging

NACA 0012, is evaluated to characterize the performance of the estimator for various flow conditions. Various sources of estimation error are analyzed and we suggest strategies to identify them. These results have been published in [30] and [31].

The contributions of the study of the vortex-cylinder system are (1) the design of a state-feedback control for a surging and/or heaving cylinder that exponentially stabilizes any of the equilibrium points of the system; and (2) the corresponding analysis of local bifurcations that arise under variation of the closed-loop control gains. Simulations of the open- and closed-loop system illustrate these bifurcations and the corresponding vortex trajectory. These results have been accepted for publication in American Control Conference 2019 [32]. Phase portraits for the vortex-airfoil system in the open and closed-loop cases are presented for comparison with the vortex-cylinder system.

1.4 Thesis Outline

The thesis is organized as follows: Chapter 2 provides background information for the results presented in further chapters, Chapter 3 presents the DMD and DMD-KF results. Chapter 4 presents the analysis of the cylinder-vortex and airfoil-vortex systems. Chapter 5 summarizes contributions and suggests future work.

Section 2.1 provides an overview of potential flow modeling and derives the equations of motion of a single vortex near an actuated cylinder. Section 2.2 summarizes DMD, DMDSP, and DMD-KF.

Section 3.1 describes the implementation of the DMDSP algorithm on two

experimental data sets, including an overview of the process of selecting the number of DMD modes. Section 3.2 evaluates the DMD-KF performance via comparison to the original and DMD reconstructed data. Section 3.3 summarizes the DMD-KF results.

Section 4.1.1 presents the various flow topologies of the open-loop system that result from the choice of system parameters. Section 4.1.2 analyzes the stability of the equilibrium points of the closed-loop system, gives conditions on the feedback gains to achieve exponential stability, and presents simulation results. Section 4.1.3 summarizes the results for the cylinder-vortex system. Section 4.2.1 presents the equilibrium points and sample trajectories for the airfoil-vortex system. Section 4.2.2 presents results of applying feedback control to stabilize the airfoil-vortex system. Section 5.1 summarizes the contributions of the thesis and Section 5.2 suggests future work.

Chapter 2: Background

2.1 Potential Flow Modeling

The potential flow model assumes the fluid is incompressible and irrotational. Under this assumption, the fluid velocity can be obtained as the gradient of a potential function [33]. The advantage of potential flow is that the solution can be decoupled as a sum of elementary flows such as point sources, sinks, vortices, doublets, and uniform flow. For example, a cylinder in uniform flow can be described as a doublet in a uniform field. This configuration forms a cylinder-shaped streamline which separates the flow into two regions in the same way the surface of the cylinder does.

Detached flow structures arise due to viscous effects and contain vorticity (i.e. the flow is not irrotational). Despite this, potential flow is useful to model detached flow because the transportation of vorticity is mostly driven by convection instead of diffusion [14]. The vorticity is contained in a point vortex, vortex sheet or vortex patch that convects according to the flowfield at the vortex position minus the flowfield of the vortex itself.

2.1.1 Dynamics of a point vortex near a cylinder

In this work, the vorticity is modeled as a single point vortex. Consider a cylinder of radius r_0 centered at z_0 , a vortex of strength Γ_v located at z , and a freestream velocity u_∞ , where $z, z_0, u_\infty \in \mathbb{C}$ and the real and imaginary components correspond to x and y components, respectively. The potential for the freestream flow around the cylinder consists of a uniform flow, a doublet, and a vortex placed at the center of the cylinder [33]. The strength Γ_0 of the vortex placed at the center of the cylinder (from now on referred to as the bound vorticity) is a free parameter since any value obeys the boundary conditions of the flow. Let $*$ denote complex conjugation. The flow felt by the vortex corresponds to that of the freestream around a cylinder with a bound vortex plus that of an image vortex of opposite strength placed at [34]

$$z_{im} = z_0 + \frac{r_0^2}{(z_v - z_0)^*}. \quad (2.1)$$

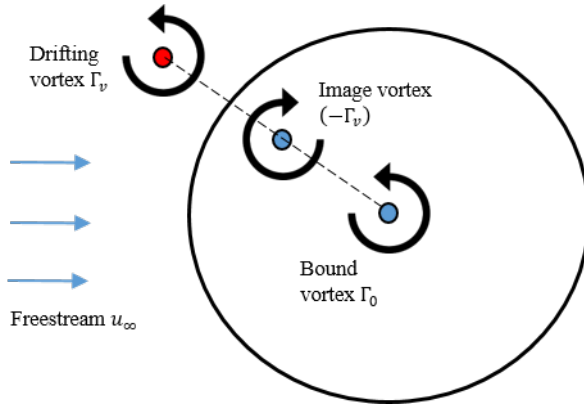


Figure 2.1: The drifting vortex is convected by the influence of the freestream, the cylinder, the image vortex, and the bound vortex.

The equations of motion are derived using a complex potential. The potential $F(z)$ for the flow with a vortex placed at z_v , is

$$F(z) = u_\infty^* z + \frac{u_\infty r_0^2}{z - z_0} + \frac{\Gamma_0}{2\pi i} \log(z - z_0) - \frac{\Gamma_v}{2\pi i} \log(z - z_{im}) + \frac{\Gamma_v}{2\pi i} \log(z - z_v). \quad (2.2)$$

The potential that describes the time evolution of the vortex position, is the potential of the flow minus the potential of the vortex itself, i.e.,

$$F^{-v}(z) = F(z) - \frac{\Gamma_v}{2\pi i} \log(z - z_v). \quad (2.3)$$

The time evolution of the vortex position is given by the conjugate gradient of $F^{-v}(z)$ evaluated at the position of the vortex [35] i.e.,

$$\dot{z}_v = \left(\frac{dF^{-v}(z)}{dz} \Big|_{z=z_v} \right)^* = u_\infty - u_\infty^* \frac{r_0^2}{((z_v - z_0)^2)^*} + \frac{i\Gamma_0}{2\pi} \frac{z_v - z_0}{|z_v - z_0|^2} - \frac{i\Gamma_v}{2\pi} \frac{z_v - z_0}{|z_v - z_0|^2 - r_0^2}. \quad (2.4)$$

2.1.2 Dynamics of a Point Vortex Near an Actuated Airfoil

The flow around an arbitrary shape can be found using a conformal mapping. A conformal mapping is an angle preserving transformation which, in this context, maps a cylinder to an arbitrary shape [35]. The potential function around a cylinder can then be used to find the potential around a new shape such as a Joukowski airfoil, a type of airfoil which is of theoretical interest because its shaped is obtained

by a simple conformal mapping known as the Joukowski transform.

The dynamics for a point vortex in the presence of an airfoil differ from the cylinder due to the conformal mapping, the imposition of the Kutta condition, and the Rouge correction. The Joukowski transform, may induce an asymmetry that breaks the results obtained for the equilibrium conditions for the cylinder. The Kutta condition states that the flow leaves tangentially to the separating edge. This condition forces a specific value for the circulation around the airfoil, as opposed to the cylinder in which different values for the circulation are valid solutions [36]. The Rouge correction is a term that arises due to the subtraction of the potential due to the free vortex, which is not trivial when using the Joukowski transform [37].

2.1.2.1 Joukowski Transform

Let $g(z)$ represent the mapping function

$$\zeta = g(z) = z + a^2/z. \quad (2.5)$$

z is the coordinate in the circle plane. ζ is the coordinate in the airfoil plane. Consider a circle of radius $r_0 = a(1 + c)$ centered at $z_0 = -ac$ and $a, c \in \mathbb{R}$. The circle maps to a Joukowski airfoil with a sharp trailing edge at $z = a \rightarrow \zeta = 2a$ [38].

2.1.2.2 Kutta condition

The Kutta condition requires the flow velocity in the circle plane at the trailing edge to be 0. Can also be written as [38]

$$\left. \frac{dF}{dz} \right|_{z=a} = 0. \quad (2.6)$$

Replacing in (2.2)

$$\begin{aligned} 0 &= u_\infty e^{-i\alpha} - u_\infty e^{i\alpha} \frac{a^2(1+c)^2}{(a^2(1+c)^2)} + \frac{\Gamma_0}{2\pi i} \frac{1}{a(1+c)} + \frac{\Gamma_v}{2\pi i} \left(\frac{1}{a-z_v} - \frac{1}{a(1+c) - \frac{a^2(1+c)^2}{(z_v^*+ac)}} \right) \\ 0 &= 2\pi i u_\infty (e^{-i\alpha} + e^{i\alpha}) + \Gamma_v \left(\frac{(z_v^*+ac)(a(1+c) - a^2(1+c)^2 - (a-z_v)(z_v^*+ac))}{(a-z_v)(a(1+c)(z_v^*+ac)) - a^2(1+c)^2} \right) \\ &\quad + \frac{\Gamma_0}{a(1+c)} \\ 0 &= 4\pi a(1+c)u_\infty \sin(\alpha) + \Gamma_v \left(\frac{(z_v^*+ac)(z_v+ac) - a^2(1+c)^2}{(a-z_v)(z_v^*-a)} \right) + \Gamma_0 \\ \Gamma_0 &= -4\pi a(1+c)u_\infty \sin(\alpha) + \Gamma_v \frac{|z_v+ac|^2 - a^2(1+c)^2}{|z_v-a|^2} \end{aligned} \quad (2.7)$$

The term that accompanies Γ_v ranges from 0 near the surface of the cylinder (except near the trailing edge) to ∞ near the trailing edge and is always positive. It goes to 1 far away from the cylinder. Figure 2.2 shows the geometrical relation between this terms to ease visualization.

2.1.2.3 Routh correction

Let $F_c(z)$ be the complex potential in the circle plane. It can be split as

$$F_c(z) = F_c^{-v}(z) + \frac{\Gamma_v}{2\pi} \log(z - z_v) \quad (2.8)$$

where $F_c^{-v}(z)$ is the complex potential for everything (Free stream, bound vortex,

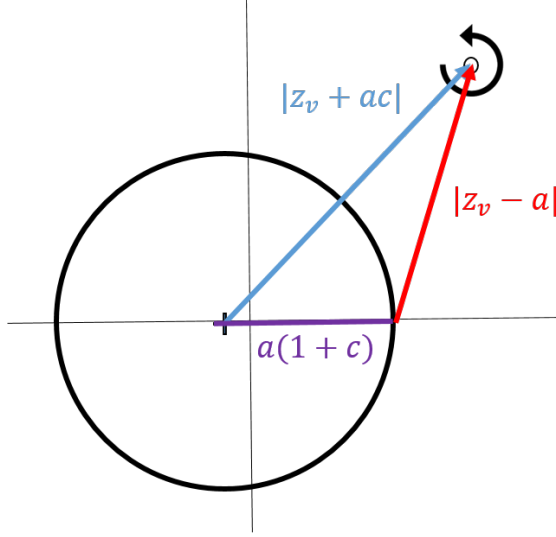


Figure 2.2: Geometrical relation between terms of (2.7).

image vortex) except the free vortex itself.

The complex potential at corresponding z and ζ points are equal [37].

$$\begin{aligned}
 F_a(\zeta) &= F_c(z) \\
 F_a^{-v}(\zeta) + \frac{\Gamma_v}{2\pi i} \log(\zeta - \zeta_v) &= F_c^{-v}(z) + \frac{\Gamma_v}{2\pi i} \log(z - z_v) \\
 F_a^{-v}(\zeta) &= F_c^{-v}(z) + \frac{\Gamma_v}{2\pi i} \log\left(\frac{z - z_v}{g(z) - g(z_v)}\right).
 \end{aligned} \tag{2.9}$$

Then derive and set $\zeta = \zeta_v$ to find the complex velocity.

$$\begin{aligned}
 \frac{dF_a^{-v}(\zeta_v)}{d\zeta} &= \lim_{z \rightarrow z_v} \frac{d}{d\zeta} \left[F_c^{-v}(z) + \frac{\Gamma_v}{2\pi i} \log\left(\frac{z - z_v}{g(z) - g(z_v)}\right) \right] \\
 &= \frac{dz}{d\zeta} \left[\frac{dF_c^{-v}(z_v)}{dz} + \lim_{z \rightarrow z_v} \frac{d}{dz} \left(\frac{\Gamma_v}{2\pi i} \log\left(\frac{z - z_v}{g(z) - g(z_v)}\right) \right) \right] \\
 &= \frac{1}{\frac{dg}{dz}} [w_c^{-v}(z_v) + R].
 \end{aligned} \tag{2.10}$$

The first term inside the brackets is identical to the complex velocity of a vortex near a cylinder. The second term is known as the Routh correction and evaluates

to [38]:

$$R = \frac{i\Gamma_v}{2\pi} \frac{\frac{d^2g}{dz^2}}{2\frac{dg}{dz}} = \frac{i\Gamma_v}{2\pi} \frac{a^2}{z_v(z_v^2 - a^2)} \quad (2.11)$$

The convection velocity for a vortex near an airfoil is the complex conjugate of (2.10).

$$\dot{\zeta}_v = \frac{1}{\left(\frac{dg}{dz}\right)^*} (w_c^{-v*} + R^*) \quad (2.12)$$

The term w_c^{-v*} is identical to \dot{z}_v in (2.4), however z_v in (2.4) has dynamics different from z_v in (2.10), even if Γ_0 is replaced by the Kutta condition. To prove this, Let $z_{v,c}$ have dynamics defined by (2.4), i.e. $\dot{z}_{v,c} = w_c^{-v*}$, and $z_{v,a}$ be the z_v used in this Section, i.e. $\dot{\zeta}_v = g(z_{v,a})$. The definition of $z_{v,a}$ implies

$$\begin{aligned} \dot{\zeta}_v &= \frac{dg}{dz} \dot{z}_{v,a} \\ \dot{z}_{v,a} &= \left(\frac{dg}{dz}\right)^{-1} \dot{\zeta}_v \\ &= \left|\frac{dg}{dz}\right|^{-2} (\dot{z}_{v,c} + R^*) \\ &= \left|\frac{z^2}{z^2 - a^2}\right|^2 \left(\dot{z}_{v,c} + \left[\frac{i\Gamma_v}{2\pi} \frac{a^2}{z(z^2 - a^2)}\right]^*\right) \\ \dot{z}_{v,a} &= \left|\frac{z^2}{z^2 - a^2}\right|^2 \left(\dot{z}_{v,c} - \frac{i\Gamma_v}{2\pi} \frac{a^2(z^3 - za^2)}{|z|^2|z^2 - a^2|^2}\right). \end{aligned} \quad (2.13)$$

By setting $\Gamma_v = 0$ it is trivial to see $\dot{z}_{v,a} \neq \dot{z}_{v,c}$. The conformal mapping is a way to obtain the dynamics of the vortex in the airfoil plane, not a coordinate transform between two equivalent dynamical systems. However we do want to work on the circle plane and make it equivalent to the dynamics of a vortex near an airfoil which is why we will use the variable $\dot{z}_{v,a}$. Compared to the dynamics near a circle, there are three new effects at play. The first is the Kutta condition, which fixes

Γ_0 as a function of the angle of attack, the freestream velocity and the strength and position of the free vortex. The second is Routh correction, which adds a new term in the dynamics and the third is a scaling factor which makes speeds near the trailing edge very high. The scaling factor is not of great interest because it won't affect the equilibrium points or the shape of the trajectories.

2.2 Dynamic Mode Decomposition

DMD is a data-driven algorithm to compute the eigenvalues and eigenmodes of a linear model that approximates the dynamics of data [39]. There are many variations of and additions to DMD [40]. This thesis uses Schmid's algorithm [12] to obtain the DMD modes and eigenvalues and DMDS by Jovanović, Schmid and Nichols [21] to select the most relevant modes for a reduced-order model. The Koopman Observer Form by Surana and Banaszuk [13] creates an observer matrix for the reduced-order model to be used in the DMD-KF for estimation [41].

2.2.1 Base algorithm

Consider a dataset of $m + 1$ snapshots, where each snapshot corresponds to a vector of observables $\boldsymbol{\psi}(t_k) \in \mathbb{R}^n$ at time step k for $k = 1, \dots, m+1$. The time between steps must be constant, i.e., $t_{k+1} - t_k = \Delta t$. It is common for n (the dimension of the snapshot vector) to be much bigger than $m + 1$ (the number of snapshots). For example, in fluids simulations or PIV data there are often more measurements than time steps. Form two matrices with these snapshots; the columns of these matrices

contain the snapshot sequence, offset by one time step, such that

$$\Psi = \begin{bmatrix} | & & | & & & & | \\ \psi(t_1) & \psi(t_2) & \cdots & \psi(t_{m-1}) & & & \\ | & & | & & & & | \end{bmatrix} \quad \text{and} \quad \Psi' = \begin{bmatrix} | & & | & & | \\ \psi(t_2) & \psi(t_3) & \cdots & \psi(t_m) & \\ | & & | & & | \end{bmatrix}. \quad (2.14)$$

DMD is an eigendecomposition of a linear operator A that approximates the dynamics that evolve the system one step forwards in time, i.e., $\Psi' = A\Psi$. The best fit for this operator can be found using the pseudoinverse \dagger , so $A = \Psi'\Psi^\dagger$. However, if $n \gg m$, this approach may not be practical. Instead, the eigenvalues and eigenvectors of A are obtained without computing A explicitly, using a projected version of A . Consider the Singular Value Decomposition (SVD)

$$\Psi = U\Sigma V^*, \quad (2.15)$$

where $*$ indicates the conjugate transpose. The columns of U form the POD modes of the data set Ψ . The pseudoinverse of the SVD satisfies $\Psi^\dagger = V\Sigma^{-1}U^*$, which implies

$$A = \Psi'V\Sigma^{-1}U^*. \quad (2.16)$$

\tilde{A} is a low-dimensional projection onto the POD basis [12] defined by the columns of U , i.e.,

$$\tilde{A} = U^*AU = U^*\Psi'V\Sigma^{-1}. \quad (2.17)$$

If $m < n$, computing the eigendecomposition of \tilde{A} ($m \times m$) is easier than computing the eigendecomposition of A ($n \times n$). Let Λ be the diagonal matrix of eigenvalues of \tilde{A} and W the matrix of right eigenvectors of \tilde{A} . The eigenvalues of A are the same as the eigenvalues of \tilde{A} [42] and represent the DMD eigenvalues. The matrix of DMD modes

$$\Phi = UW \quad (2.18)$$

corresponds to the approximate eigenvectors of A [42]. Note that the DMD modes in (2.18) are a linear combination of POD modes.

Let the vector $\boldsymbol{\alpha}(t)$ of DMD mode amplitudes denote the approximate representation of the vector $\boldsymbol{\psi}(t)$ of observables in the DMD-mode basis, so $\boldsymbol{\psi}(t) \approx \Phi\boldsymbol{\alpha}(t)$. The time evolution is $\boldsymbol{\alpha}(t_{k+1}) = \Lambda\boldsymbol{\alpha}(t_k)$, which implies the approximate solution for the dynamics of the vector observable is [40]

$$\boldsymbol{\psi}(t) \approx \Phi\boldsymbol{\alpha}(t) = \Phi\Lambda^{(t-t_1)/\Delta t}\boldsymbol{\alpha}(t_1), \quad (2.19)$$

where $\Delta t = t_{k+1} - t_k$. Using the decomposition (2.18) and (2.19) allows us to approximate the original data or data coming from the same dynamical system, but with different initial conditions. If the underlying system is linear, the DMD modes and eigenvalues are inherent to the dynamics, whereas the mode amplitudes depend on the initial conditions. If the system is nonlinear, the modes and eigenvalues

may change with the initial conditions of the dataset. However, for the purpose of estimation, we assume that the modes found are representative of and inherent to the underlying dynamics. Whether or not this assumption is valid depends on how nonlinear the system is and how representative the dataset is of the trajectories to be estimated.

2.2.2 Sparsity Promoting Dynamic Mode Decomposition

In the case of an oscillatory flow, a small number of DMD modes often provides a sufficiently accurate reconstruction of the data [3]. To find those modes and their initial amplitudes, we employ the Sparsity Promoting DMD (DMDSP) algorithm developed by Jovanović, Schmid and Nichols [21], which consists of finding the mode amplitudes that minimize the cost function

$$J_\gamma(\boldsymbol{\alpha}(t_1)) = \sum_{k=1}^m \|\boldsymbol{\psi}(t_k) - \Phi \Lambda^{t_k/\Delta t} \boldsymbol{\alpha}(t_1)\|^2 + \gamma |\alpha_k(t_1)|. \quad (2.20)$$

The first term in (2.20) corresponds to the difference between the original data and the DMD reconstruction, the second term is a penalty on non-zero mode amplitudes, and γ is a positive parameter that weights this penalty. After minimizing (2.20) for a particular value of γ , the modes with non-zero amplitudes are the modes chosen for the reconstruction; these modes correspond to the most influential modes. Then (2.20) is minimized again with $\gamma = 0$, using only the chosen modes, to obtain the optimal mode amplitudes to reconstruct the data with the reduced set of modes [21].

Although fewer modes yield a less accurate reconstruction, only certain modes may reproduce the dynamics of the system with sufficient accuracy. The value of γ dictates the number m^* of chosen modes, so it represents the desired balance between the number of modes and the quality of the reproduction [21]. This process is illustrated in Section 3.1.

2.2.3 Dynamic Mode Decomposition Kalman Filter

DMDSP identifies the mode amplitudes that best fit a time series of training data. Determining the DMD mode amplitudes provides an estimate of the data, even in real time. A Kalman filter is a dynamic observer that gives real-time estimates of the system state using a dynamic model and noisy (linear) measurements from sensors. This section describes a method to estimate the mode amplitudes and thus the whole data set from a subset of the measurements. Based on the Koopman Observer Form [13], the main idea is to use DMD on the training data to generate a linear dynamical system that represents the dynamics we observe and to use a Kalman Filter to estimate this system from sensor measurements in the test data.

When constructing the snapshot matrices from the training data, every snapshot $\psi(t_k)$ must contain the states ($\mathbf{x} \in \mathbb{R}^{n_x}$) to be estimated concatenated with the observables ($\mathbf{y} \in \mathbb{R}^{n_y}$) that will be readily available as measurements. Here, \mathbf{x} corresponds to PIV measurements and \mathbf{y} corresponds to pressure sensor measurements, although this formulation is otherwise general. The snapshot matrices are

$$\Psi = \begin{bmatrix} | & & | \\ \mathbf{x}(t_1) & \cdots & \mathbf{x}(t_m) \\ | & & | \\ \hline | & & | \\ \mathbf{y}(t_1) & \cdots & \mathbf{y}(t_m) \\ | & & | \end{bmatrix} \quad \Psi' = \begin{bmatrix} | & & | \\ \mathbf{x}(t_2) & \cdots & \mathbf{x}(t_{m+1}) \\ | & & | \\ \hline | & & | \\ \mathbf{y}(t_2) & \cdots & \mathbf{y}(t_{m+1}) \\ | & & | \end{bmatrix}. \quad (2.21)$$

Next, apply the DMD and DMDSF algorithms to obtain a tuple of m^* DMD eigenvalues (λ_i) and DMD modes (ϕ_i) and arrange them so complex conjugates are grouped together. The amplitudes obtained from DMDSF are not required to create a DMD-based observer, however it is useful to have as reference the best possible reconstruction using the chosen set of modes. The modes and eigenvalues are similar but slightly different from those obtained by performing DMD on only the PIV data. A weighting can be applied to give more emphasis to the states to estimate (\mathbf{x}) or the measurements (\mathbf{y}), but this idea was not explored in this thesis. Instead, all quantities were nondimensionalized so their magnitudes are comparable. Form observation matrix C by letting C_i be the i th column of C with [13]

$$C_i = \phi_i, \text{ if } \phi_i \text{ is real, and} \quad (2.22)$$

$$C_i = \text{Re}(\phi_i) \text{ and } C_{i+1} = \text{Im}(\phi_i), \text{ if } \phi_i \text{ and } \phi_{i+1} \text{ are complex conjugates.}$$

Form the dynamics matrix F as a block diagonal matrix such that F has a diagonal entry $F_{i,i} = \lambda_i$, if λ_i is real, and block diagonal entry [13]

$$\begin{bmatrix} F_{i,i} & F_{i,i+1} \\ F_{i+1,i} & F_{i+1,i+1} \end{bmatrix} = \begin{bmatrix} \operatorname{Re}(\lambda_i) & \operatorname{Im}(\lambda_i) \\ -\operatorname{Im}(\lambda_i) & \operatorname{Re}(\lambda_i) \end{bmatrix}, \quad (2.23)$$

if λ_i and λ_{i+1} are complex conjugates. Split C into C_x and C_y , corresponding to the first n_x and the last n_y rows of C , respectively.

Let z denote the vector of DMD amplitudes expressed in block modal form.

These matrices define the linear dynamical system [13]

$$\mathbf{z}_k = F \mathbf{z}_{k-1} \quad (2.24a)$$

$$\mathbf{y}_k \approx C_y \mathbf{z}_k \quad (2.24b)$$

$$\mathbf{x}_k \approx C_x \mathbf{z}_k. \quad (2.24c)$$

If the system given by equations (2.24a) and (2.24b) is observable, then a linear state observer such as a Kalman filter will estimate the state \mathbf{z} given measurements \mathbf{y} .

The Kalman filter is the optimal algorithm to estimate the states of a linear system subject to Gaussian process noise with covariance Q and measurement noise with covariance R [41]. It involves propagating the current estimate $\hat{\mathbf{z}}$ and covariance P of the current estimate in time using knowledge of the dynamics and updating these values based on measurements. In this particular implementation, an extra step is added to compute the estimate of \mathbf{x} using (2.24c). Given the system described

by (2.24), the filter equations are [41]

$$\text{Estimate Propagation} \quad \hat{\mathbf{z}}_k^- = F \hat{\mathbf{z}}_{k-1} \quad (2.1a)$$

$$P_k^- = F P_{k-1} F^T + Q \quad (2.1b)$$

$$\text{Kalman Gain} \quad K_k = P_k^- C_y (C_y P_k^- C_y^T + R)^{-1} \quad (2.1c)$$

$$\text{Assimilating measurements} \quad \hat{\mathbf{z}}_k = \hat{\mathbf{z}}_k^- + K(y_k - C_y \hat{\mathbf{z}}_k^-) \quad (2.1d)$$

$$P_k = (I - K C_y) P_k^- \quad (2.1e)$$

$$\text{Estimate of } \mathbf{x} \quad \hat{\mathbf{x}}_k = C_x \hat{\mathbf{z}}_k. \quad (2.1f)$$

The superindex $-$ refer to the estimate before assimilating measurements. The symbol $\hat{}$ indicates the quantity is an estimate, not the true value.

2.2.4 Sources of Error in the Dynamic Mode Decomposition Kalman Filter

The system dynamics (2.24) can be written as

$$\mathbf{x}_{k+1} = C_x F C_x^\dagger \mathbf{x}_k + \mathbf{w}_k; \quad \mathbf{y}_k = C_y C_x^\dagger \mathbf{x}_k + \mathbf{v}_k. \quad (2.1)$$

The process noise \mathbf{w}_k and measurement noise \mathbf{v}_k include the inherent noise from the dynamics and the loss of information due to the approximation. The process noise can be split into components either in, or orthogonal to, the span of DMD modes:

i.e.,

$$\mathbf{w}_{k,\parallel} = C_x C_x^\dagger \mathbf{w}_k; \quad \mathbf{w}_{k,\perp} = \mathbf{w}_k - \mathbf{w}_{k,\parallel}. \quad (2.2)$$

The terms $\mathbf{w}_{k,\parallel}$ and \mathbf{v}_k correspond to the process and measurement noise in the reduced-order model and are related to the uncertainty induced by assuming a linear model for the reduced order dynamics. We compute Q and R as

$$Q = \text{Cov} [C_x^\dagger x_{k+1} - F C_x^\dagger x_k]; \quad R = \text{Cov} [y_k - C_y C_x^\dagger x_k]. \quad (2.3)$$

In contrast, $\mathbf{w}_{k,\perp}$ is unrelated to the filtering process and corresponds to the inability of the chosen DMD modes to account for the variability in the states to be estimated. The DMD-KF will only produce estimates in the span of the DMD modes, so the best possible estimate for the state, in the least squares sense, is $\tilde{\mathbf{x}} = C_x C_x^\dagger \mathbf{x}$. We denote this quantity as the *DMD projection*. The DMD projection is useful to quantify the information lost from projecting into a low-dimensional model.

Distinguish between three ways to recreate the evolution of a flowfield from a modal decomposition: projection, reconstruction, and estimation. *Projection* refers to projecting the test data into the span of the modes generated from the training data. This process yields the least possible ℓ_2 norm of the difference between the instantaneous test data snapshot and a representation in terms of the selected modes, and thus can serve as a lower bound for the error. *Reconstruction* refers to finding the initial mode amplitudes that produce a trajectory, given by (2.19) (i.e., propagation of DMD modes assuming no process noise), which minimizes the difference from the

test data. *Estimation* refers to the result of implementing a DMD-KF to obtain an approximation of the test data using only a limited set of measurements. A large difference between the projection and the reconstruction may indicate a large process noise covariance, which can be attributed to inherently noisy dynamics or a flawed dynamic model. If the reconstruction error is small, but the estimation error is large, the problem may be due to a flawed measurement model.

2.2.5 More concepts in DMD

DMD has a close relationship with an operator-theoretic description of dynamical systems based on the Koopman operator [43]. The Koopman operator advances observables of a dynamical system linearly in time [44]. It serves as a way to represent a finite-dimensional nonlinear system as an infinite dimensional linear system [44]. If the DMD modes are able to correctly approximate the Koopman modes of the underlying dynamics, then the DMD-KF is equivalent to the Koopman Kalman Filter (KKF) [13].

Chapter 3: Data Driven Estimation of Unsteady Flowfield near an Actuated Airfoil

3.1 Dynamic Mode Decomposition on an Actuated Airfoil

This section describes the application of the DMD and DMDS procedures described in Sections 2.2.1 and 2.2.2 to two different experimental datasets from airfoils in periodic unsteady flow conditions. Using two separate experiments allows us to test the algorithm in a wider variety of conditions. These datasets were obtained from previously unrelated work by the STAL research laboratory at University of Maryland [45] [46]. Both datasets consist of a time series of phase-averaged PIV data and pressure data from sensors embedded in the airfoils. Phase averaging means that several actuation cycles were done experimentally, then data corresponding to the same phase at different cycles was averaged together to produce a single cycle. This procedure reduces the noise in the data, but it also smooths out flow features that do not occur periodically. Getting rid of such features may or may not be desirable, but analyzing them is beyond the scope of this thesis. We refer to these phase-averaged datasets as the training datasets, as these are the sets from which the DMD modes for the DMD-KF are obtained.

Experiment 1 consists of a pitching cambered ellipse in reverse flow, with 17 pressure sensors on the suction side of the airfoil and 13 pressure sensors on the high pressure side [45]. The states to estimate correspond to the velocity components at predetermined grid points in the airfoil frame of reference. Since the airfoil was pitching while the PIV cameras were stationary, the region around the airfoil where data was gathered varied during the pitching cycle. DMD requires information about every state in every snapshot, so only the points for which there is data during the entire pitching cycle are included in the area of interest shown in Figure 3.1a, which is the largest area fixed in the body frame that remains in the field of view throughout a complete pitching cycle. Table 3.2 lists the parameters used in the experiments.

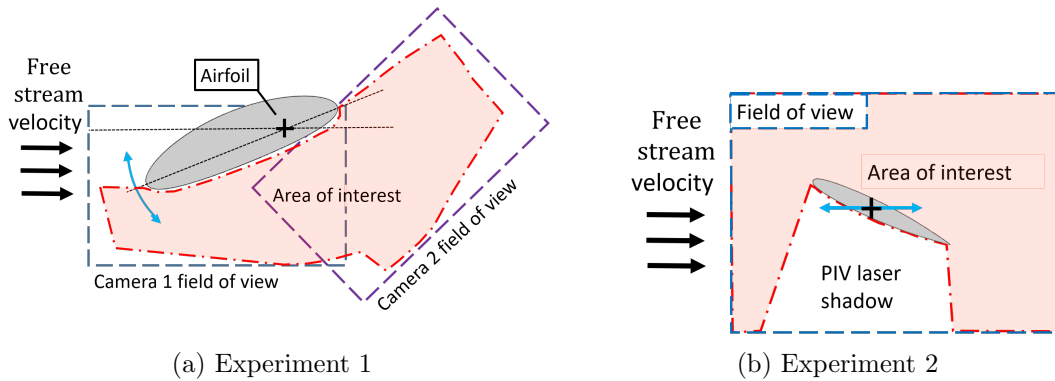


Figure 3.1: Configuration of Experiments 1 [45] and 2 [46]. Teal arrows indicate direction of actuation

Experiment 2 consists of a surging NACA 0012 airfoil with 8 pressure sensors on the suction side of the airfoil [46]. The Experiment 2 data set includes four different cases that vary the reduced frequency (k) and amplitude (Amp) of the surging motion, as shown in Figure 3.2. The amplitude is relative to the nominal Reynolds

Parameter	Experiment 1 [45]	Experiment 2 [46]
Reynolds number	165000	40000
Free stream velocity	11.9 m/s	0.34m/s
Angle of attack	180°–200°	25°
Airfoil	Cambered ellipse	NACA 0012
Actuation	Pitching sinusoidally	Surging sinusoidally
PIV data points	16907	10369
Pressure sensors	30	8
Time steps	100	84–255

Table 3.1: Summary of experimental parameters.

Case #	Amplitude ratio	Reduced frequency
1	0.25	0.160
2	0.25	0.511
3	1.0	0.160
4	1.0	0.511

Table 3.2: Actuation parameters for Experiment 2.

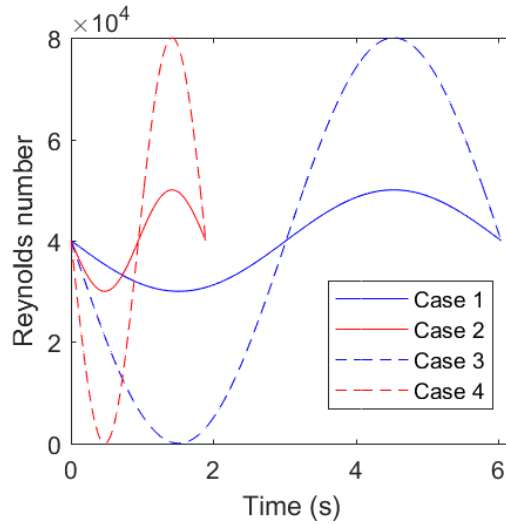


Figure 3.2: Actuation trajectories for Experiment 2.

number and the reduced frequency is the actuation frequency ω nondimensionalized by the freestream velocity v_0 and the chord length c as

$$k = \frac{\omega c}{2v_0}. \quad (3.1)$$

The first step to analyze the experimental data is to construct snapshot matrices as presented in (2.21), with \mathbf{x} corresponding to PIV measurements arranged in a column vector and \mathbf{y} corresponding to the pressure sensor data. The DMD modes and eigenvalues are obtained following the algorithm described in Section 2.2.1. This algorithm produces m DMD modes, where $m + 1$ is the number of time steps in the data, which is usually more than needed to accurately represent the system dynamics. Using fewer modes makes the estimation process run faster, so it is desirable to use only a small number of relevant modes. The DMDS algorithm described in Section 2.2.2 is used for this purpose. Varying the sparsity promoting parameter γ provides a wide range of different mode numbers. Part of the DMDS algorithm involves reconstructing the training data, which consists of finding the mode amplitudes that minimize the square of the difference between (2.19) evaluated at every time step and the original data. The reconstruction is important because it provides the best fit using (2.19) and thus can be used to evaluate if the system dynamics are well represented by a linear time evolution. The best number of modes can be chosen by looking at the accuracy of the reconstruction (Figure 3.3b), or by plotting the reconstruction and comparing it qualitatively to the training data set (Figure 3.4).

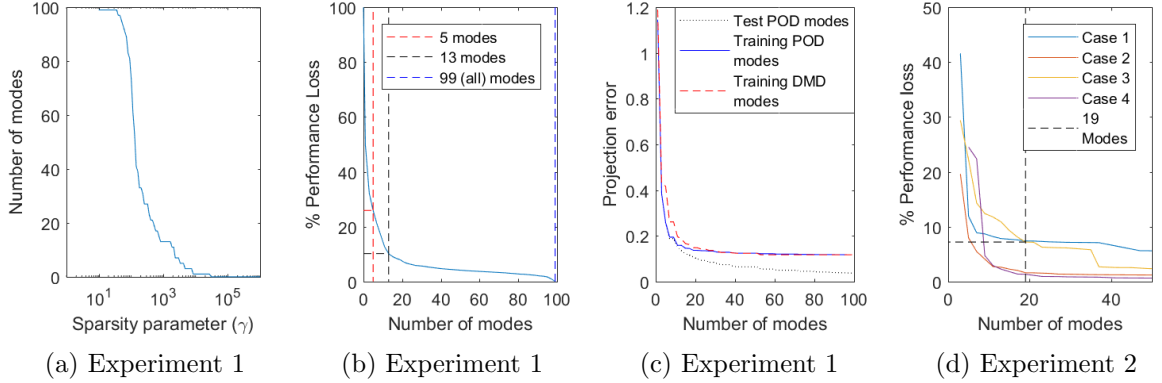


Figure 3.3: (a) Number of modes chosen by DMDS for different values of γ ; (b, d) percent performance loss versus number of modes; (c) comparison of projection error for DMD and POD modes.

Figure 3.3a shows how the number of modes changes with γ in Experiment 1. The percent performance loss from reconstruction of the data with DMD modes is defined as $100\sqrt{\frac{J_0(\alpha)}{J_0(0)}}$ [21]. Figure 3.3b shows the loss of accuracy drops rapidly between 0 and 13 modes, which implies there are diminishing returns from using additional modes. Figure 3.4 shows the original data from Experiment 1 and the reconstruction at half the actuation period, when the leading edge vortex is about to be shed. The original data and the reconstruction with all of the modes look nearly identical. In the reconstruction with 13 modes, the vortex can still be seen, but it is not as clearly defined. In the reconstruction with just five modes, the leading edge vortex does not appear; only the leading and trailing shear layers are visible.

For estimation, the chosen modes are ideally not used to represent the same data set from which the modes were obtained (the training set) but rather new data from the same dynamical system (the test set). To quantify the information lost from using a set of modes to represent a different realization of the system, we

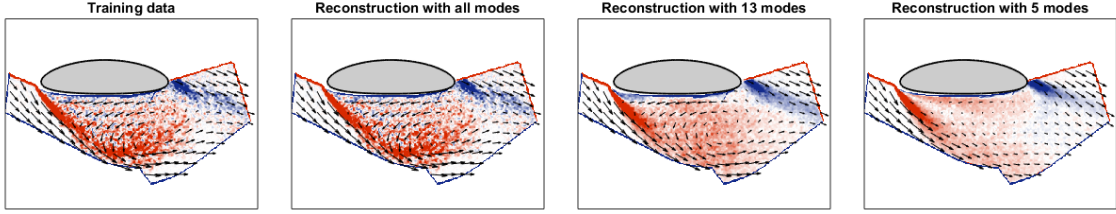


Figure 3.4: Training set data and reconstructions with different number of modes for Experiment 1 at half the actuation period ($t^*=0.5$).

compute the projection of the test set into the span of the modes obtained from the training data. Fig. 3.3c shows the projection error using DMD and POD modes of the training set and POD modes of the test set for Experiment 1. Note that the test set consists of instantaneous PIV data, representative of a case of real-time estimation. POD modes form a more accurate projection of the data; the difference corresponds to using three or four more DMD modes for the same level of accuracy, similar to the result obtained in [3]. The projection error from the POD modes of the training and test data are very close for the first 10 modes, suggesting that they contain similar information. For more modes obtained from the training set, the projection error stays almost constant. Even with the set of POD modes obtained from the test data, the projection error decreases slowly with the number of modes. Attaining an error below 5% requires over 60 POD modes.

3.2 Dynamic Mode Decomposition Kalman Filter estimation results

After an appropriate number of modes is chosen, an observer is created following the procedure described in Section 2.2.3. The DMD Kalman Filter estimates the mode amplitudes from pressure measurements in order to generate the corre-

sponding estimate of the flowfield. For illustration purposes, we use Experiment 1 to show the results of choosing different numbers of modes and Experiment 2 to present results for different actuation cases. In both experiments, the DMD-KF is designed using phase-averaged data, but for Experiment 1, the estimation is tested using both phase averaged (from the training set) and instantaneous (from the test set) measurements. For Experiment 2, the test data consists of phase-averaged measurements, so only one period is available. The time t^* indicated in the results is the time normalized by the period of the actuation.

3.2.1 Experiment 1: Pitching cambered ellipse

The DMD-KF is applied to both the training and the test data to compare performance and identify if the estimator is overfitting the data, i.e. identifying patterns in the training data that don't generalize to the test data. A plot of the estimation, reconstruction, and projection errors (defined in Section 2.2.4) over a period is used to evaluate the estimator quantitatively. A plot of the flowfield is shown to identify if flow structures are being identified properly and to evaluate the performance of the estimator qualitatively.

Figures 3.5a to 3.5c show the normalized error for the reconstruction, projection, and estimation of training data. The normalized error is defined as the average magnitude of the difference between the estimated (or reconstructed) field and the original flowfield, normalized by the average magnitude of the velocity over

the entire flowfield during the period. At the initial time step, the reconstruction and estimation differ, but then quickly converge. The error in both the estimation and reconstruction with 5 modes rises around the middle of the period, which is consistent with the reconstruction being unable to properly reproduce the leading edge vortex that is shed around this time. The error also increases when using 13 modes but not as drastically as with 5 modes. The estimation using all of the modes takes more time to converge, and does not achieve the low error of the corresponding reconstruction using all of the modes, but it does achieve the lowest error overall. A downside of using all of the modes is the increased computational time to compute the estimate, since the computational burden of computing a Kalman filter is highly dependent on the number of states [41].

Figures 3.5d to 3.5f show the corresponding normalized errors for the test data. Both the reconstruction and the estimation error increase, but the reconstruction error increased noticeably more. The reconstruction assumes no noise in the dynamics, so it is unable to correct for noisier dynamics or the difference in the evolution of the system between the test and the training data. The high value for the error in the case with 99 modes indicates that the extremely low value obtained in the reconstruction of training set data may be due to overfitting. When applied to the test data, the advantage of using more modes is lost. In fact, the reconstruction and estimation errors for 99 and 13 modes look nearly identical, which suggests that most modes beyond the first 13 may be irrelevant for reproducing the dynamics of the new data set. Because the estimation error is bounded from below by the pro-

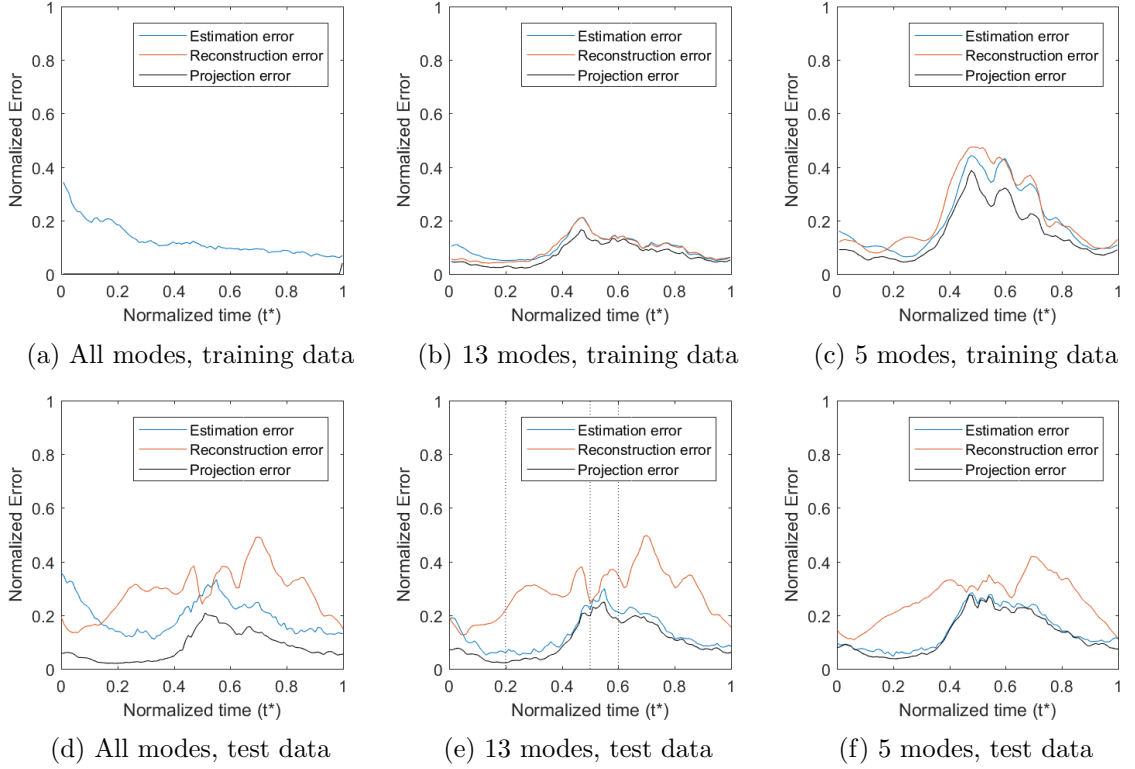


Figure 3.5: Experiment 1: Estimation, reconstruction, and projection errors. The vertical lines in (e) correspond to the frames shown in Figure 3.6.

jection error, to improve the performance, it is necessary to find a set of modes that better account for the variation in the test data. As shown in Figure 3.3c, many modes are needed to reduce the error significantly.

It is possible that the difference between the estimation and test data is not a useful metric for the performance of the estimator. The test data contains turbulent flow, which might need to be filtered out to perform feedback control based on coherent flow structures. In this case, a new error metric should quantify the filter’s ability to identify flow features useful for feedback control. Motivated by this consideration, the performance of the estimator is also studied qualitatively. Figure

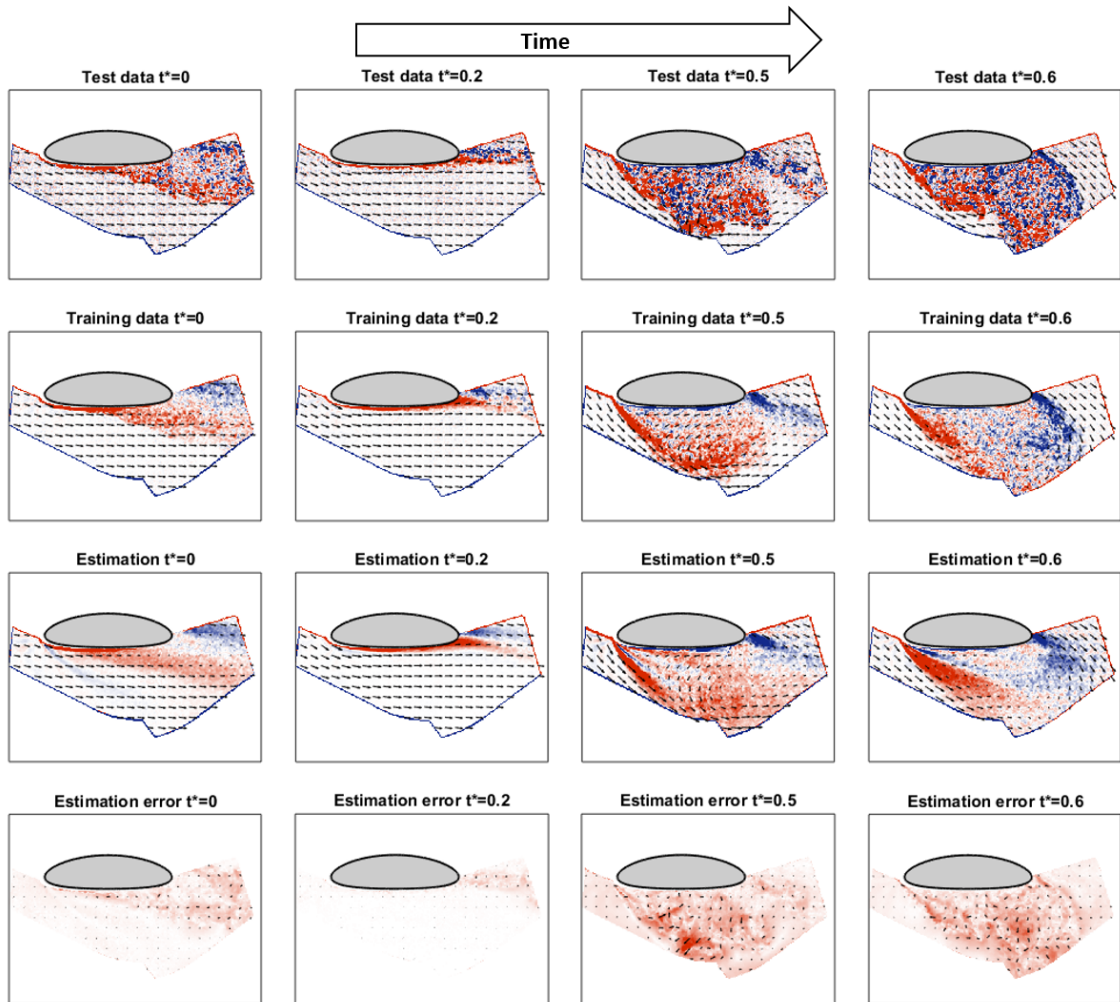


Figure 3.6: Experiment 1: Test set data, training set data, and estimate of the test data with 13 modes at several times of interest. The color red (blue) indicates positive (negative) vorticity.

3.6 shows the results of implementing a DMD-KF with 13 modes for estimation. For times $t^* = 0$ and $t^* = 0.2$, the DMD-KF is able to reproduce the test data fairly accurately. For $t^* = 0.5$, the turbulent behaviour is not captured in detail, but the main flow features, such as the shear layers and the leading edge vortex, are present in the estimate.

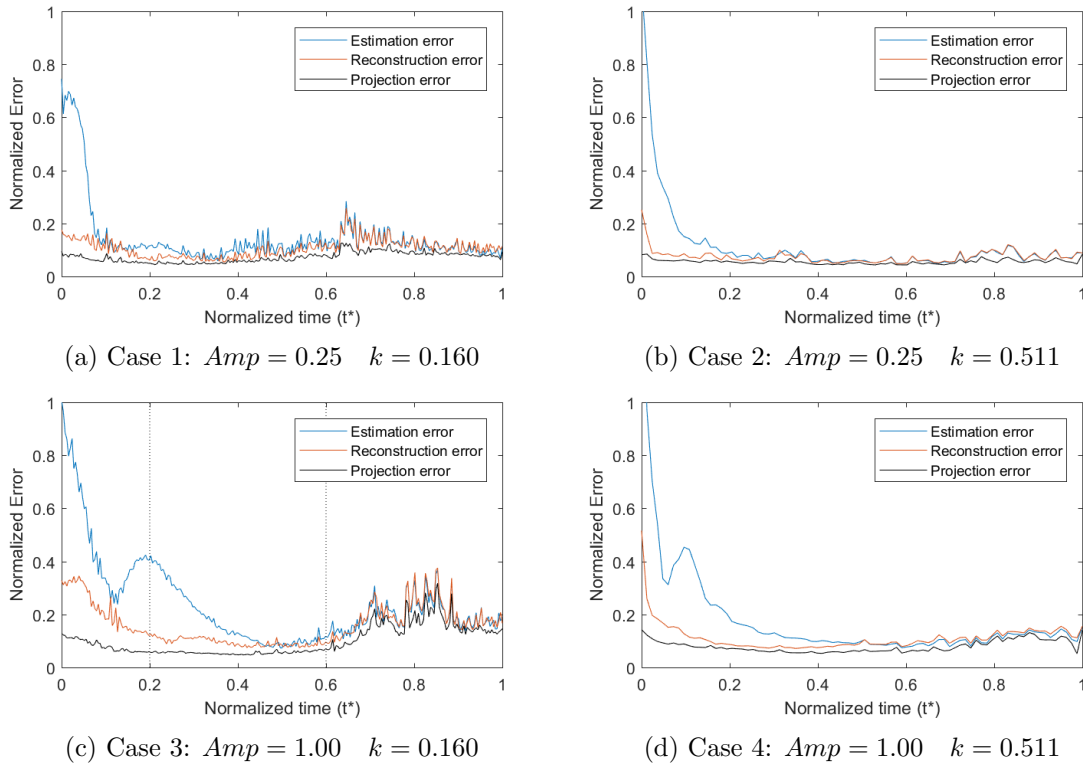


Figure 3.7: Experiment 2: Estimation, reconstruction error and projection. The vertical lines in Case 3 indicate the frames shown in Figure 3.8.

3.2.2 Experiment 2: Surging NACA 0012

The DMD-KF was applied independently to four cases of Experiment 2, with the same number of modes, for comparison purposes. The number of modes $m^* = 19$

was chosen by looking at Figure 3.3d, which shows the percent performance loss versus number of modes. There is little improvement in performance by adding more than 19 modes in any of the cases. The estimation is performed on the same data from which the DMD modes are obtained, i.e., the training and the test data are the same. This limitation in the analysis is due to the use of data from previous unrelated work, which did not collect simultaneous PIV and pressure data,

but rather phase averaged both measurements [46]. While using the same set for training and testing is not ideal, we seek here to illustrate an application of the algorithm.

Figure 3.7 shows the projection, reconstruction, and estimation error for all actuation cases in Experiment 2. In all cases, the initial estimation error is high. There are fewer sensors than modes, so the modes can not be inferred instantly, rather by comparing the predicted dynamics with the observations. The reconstruction error is also high at the initial time for most cases, whereas the projection error is low. It is possible that there are initial transients with a time evolution that is not well captured by the chosen modes. In the cases with $Amp = 1$; there is a secondary peak in estimation error; however in this case the reconstruction error is low. This result implies the system is evolving in a manner that is well approximated by the DMD linear model, but the DMD-KF is unable to completely capture the time evolution, possibly due to a flaw in the measurement model.

As a representative example, Figure 3.8 shows the flowfield for Case 3 at sev-

eral points of interest. At the initial time there are large differences, especially around the tail of the airfoil. Around $t^* = 0.2$ the flow speed is low, which might mean the flow is hard to observe; there is a peak in error observed in Figure 3.7d. Around $t^* = 0.6$, the original and the estimation look nearly identical. During the remainder of the cycle, the shedding of the leading edge vortex occurs, which is a process with increased turbulence, so it is expected that the error in both the estimate and the reconstruction are higher. Nonetheless, it is possible to see in the snapshot corresponding to $t^* = 1$ that the estimate reproduces the main features in the flow.

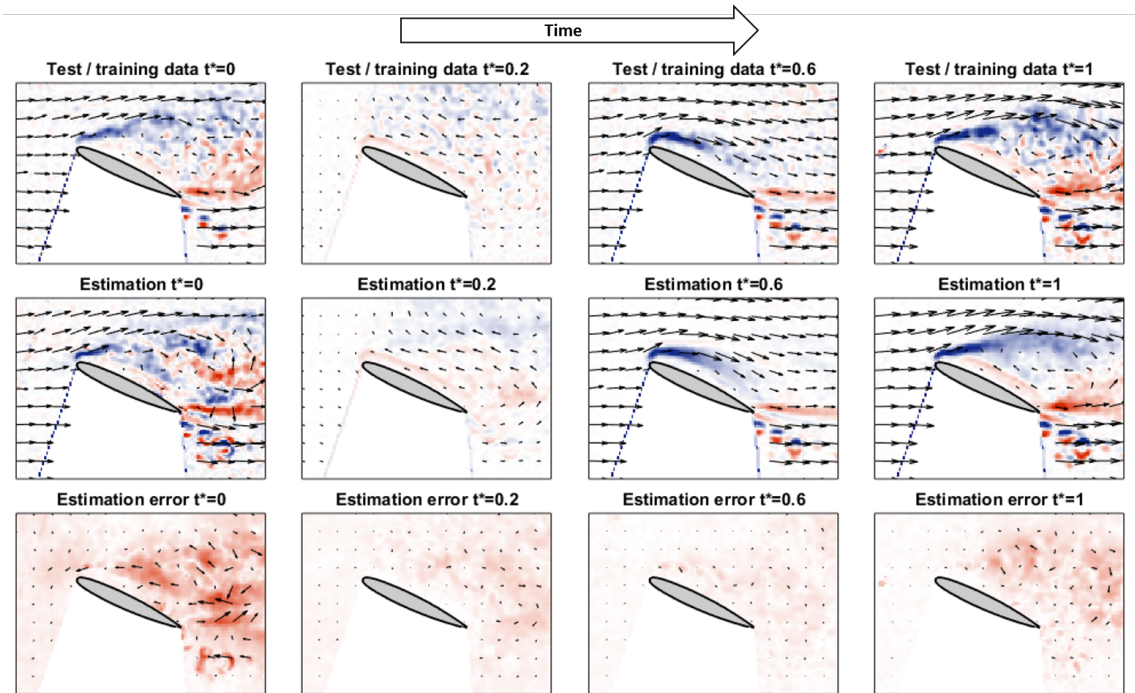


Figure 3.8: Experiment 2: Original and estimated flowfield and estimation error using 19 modes at several times of interest for case 3. For the error field, the color red indicates magnitude.

3.3 Summary

A Dynamic Mode Decomposition Kalman Filter (DMD-KF) is described to estimate the unsteady flowfield around an actuated airfoil, using information from pressure sensors. The estimation method consists of using Sparsity Promoting Dynamic Mode Decomposition (DMDSP), which finds a reduced set of dynamic modes (DMD modes) in a data set, and the Koopman Observer Form, which rewrites the modes in a form suitable for estimation, to create a linear system that approximates the dynamics of the unsteady flow. A Kalman Filter estimates the states in this linear system using pressure measurements.

The process of mode selection using DMDSP, and the effects of varying the number of modes, is illustrated using experimental results from a pitching cambered ellipse. There is a trade off with the number of modes: more modes increases the time for estimation convergence, both by increasing computational time and by taking more time steps to converge. In general, using more modes yields a better estimate, but using a small number of modes may provide a fast and accurate representation of the flowfield.

The DMD reconstruction, DMD projection, and DMD-KF estimation use DMD modes to approximate a flowfield. However the reconstruction and projection require complete knowledge of the flowfield to reproduce it with DMD modes, whereas the DMD-KF estimation uses pressure sensor measurements only. Estima-

tion error may arise from the DMD modes not spanning the features of the data to estimate, or the dynamics may not be well approximated by a linear system. The DMD projection is useful to distinguish between these sources of error, since the projection is independent of the modeled dynamics.

Chapter 4: State Feedback Stabilization of a Point Vortex near an actuated Airfoil

4.1 Dynamics of a Point Vortex Near a Cylinder

Recall from Section 2.1, the time evolution of the position of a point vortex near a cylinder is:

$$\dot{z} = u_\infty - u_\infty^* \frac{r_0^2}{(z_v - z_0)^*} + \frac{i\Gamma_0}{2\pi} \frac{z_v - z_0}{|z_v - z_0|^2} - \frac{i\Gamma_v}{2\pi} \frac{z_v - z_0}{|z_v - z_0|^2 - r_0^2}. \quad (4.1)$$

To include an input term in the dynamics, assume that u_∞ consists of a nominal freestream velocity u_0 minus the input velocity due to heaving and/or surging. For simplicity of the model, ignore unsteady aerodynamic effects so the only result of heaving and/or surging is changing the effective freestream velocity. Without loss of generality, we assume that the nominal freestream is $u_0 \in \mathbb{R}, u_0 > 0$.

To simplify the algebra, normalize length and time scales so $r_0 = 1$ and $u_0 = 1$, respectively. Define $x_1, x_2, u_1, u_2, \sigma_v, \sigma_0 \in \mathbb{R}$ such that $u_\infty = (1 - u_1 - iu_2)u_0$, $z = (x_1 + ix_2)r_0$, $\Gamma_0/2\pi = r_0u_0\sigma_0$, and $\Gamma_v/2\pi = r_0u_0\sigma_v$. x_1 and x_2 are the Cartesian coordinates of the drifting vortex, normalized by the radius of the cylinder. σ_v and σ_0 are dimensionless quantities proportional to the drifting and, respectively, bound

vortex strengths. u_1 and u_2 correspond to the surging and, respectively, heaving velocity of the cylinder, normalized by the freestream velocity. In this model, the motion of the cylinder is equivalent to a change in the freestream velocity. In non-dimensional Cartesian coordinates, the equations of motion are

$$\begin{aligned} \dot{x}_1 &= \left(\frac{x_2^2 - x_1^2}{(x_1^2 + x_2^2)^2} + 1 \right) (1 - u_1) + \frac{2x_1x_2}{(x_1^2 + x_2^2)^2} u_2 - \sigma_0 \frac{x_2}{x_1^2 + x_2^2} + \sigma_v \frac{x_2}{x_1^2 + x_2^2 - 1} \\ \dot{x}_2 &= - \frac{2x_1x_2}{(x_1^2 + x_2^2)^2} (1 - u_1) + \left(\frac{x_2^2 - x_1^2}{(x_1^2 + x_2^2)^2} - 1 \right) u_2 + \sigma_0 \frac{x_1}{x_1^2 + x_2^2} - \sigma_v \frac{x_1}{x_1^2 + x_2^2 - 1}. \end{aligned} \quad (4.2)$$

These equations are only valid in the region $x_1^2 + x_2^2 > 1$, i.e., when the vortex is outside of the cylinder.

4.1.1 Bifurcations of the Open-Loop Dynamics

The location of the equilibrium points of (4.2) and their bifurcations are found by varying σ_0 and σ_v ; a thorough description can be found in [29]. To find the zero-input equilibrium points $(\tilde{x}_1, \tilde{x}_2)$, set $\dot{x}_1 = \dot{x}_2 = u_1 = u_2 = 0$. The equilibrium points for this system always occur along the line $\tilde{x}_1 = 0$ [29], which follows from the condition $\dot{x}_2 = 0$. Solving for $\dot{x}_1 = 0$ yields the polynomial

$$\tilde{x}_2^4 + (\sigma_v - \sigma_0)\tilde{x}_2^3 + \sigma_0\tilde{x}_2 - 1 = 0. \quad (4.3)$$

Depending on the value of the parameters σ_v and σ_0 , (4.3) can have two, three, or four real solutions. One solution always lies within the unit circle, which is not

a valid equilibrium point for the system, because it is inside the cylinder. Without loss of generality, we take $\sigma_v > 0$: if $\sigma_v < 0$, we can flip the signs of σ_0, x_2 , and u_2 , i.e., reflect across the horizontal axis, and obtain the same dynamics; if $\sigma_v = 0$, the system corresponds to a free particle rather than a vortex.

With these conventions, polynomial (4.3) evaluated at $\tilde{x}_2 = -1$ is equal to $-\sigma_v < 0$, whereas in the limit $\tilde{x}_2 \rightarrow -\infty$, it is positive. Therefore, the polynomial must always have a root in the interval $(-\infty, -1)$. This equilibrium point exists for all values of σ_0 and σ_v and, in Section 4.1.2, we show that this point is always a saddle. In general, varying the σ_v and σ_0 will change the number of equilibrium points and their positions. Figure 4.1a shows the regions in parameter space for which the system has three equilibrium points: a saddle on the negative x_2 axis (the lower saddle), a saddle on the positive x_2 axis (the upper saddle), and a center on the x_2 axis between the upper saddle and the cylinder. The boundary between the regions with one and three equilibrium points corresponds to parameter values for which the system has two equilibrium points: a saddle under the cylinder and an undefined equilibrium point above the cylinder. However, this region has zero area, is not of physical interest [29], and we ignore it in the subsequent analysis.

Figure 4.1b shows a bifurcation diagram varying σ_0 with fixed $\sigma_v = 2$. Fig. 4.2a shows trajectories in the phase plane of vortex position for $\sigma_0 = 0$: there is a single saddle below the cylinder. As σ_0 increases, the saddle point moves closer to the surface of the cylinder. At the critical value, the system exhibits a saddle-node bifurcation: a new equilibrium point appears on the opposite side of the cylinder and splits into a center and a saddle, see Figure 4.2b. There is still a saddle point

below the cylinder, the separatrix comes arbitrarily close to the saddle, then wraps clockwise around the cylinder getting near the saddle again, before going off to infinity.

Below the bifurcation point, the phase portrait is split into three regions: the upper region, the lower region, and periodic orbits surrounding the cylinder. Above the bifurcation point, the upper region splits into three regions, as shown in Figure 4.2b. More phase diagram topologies for the open-loop system are described in [29].

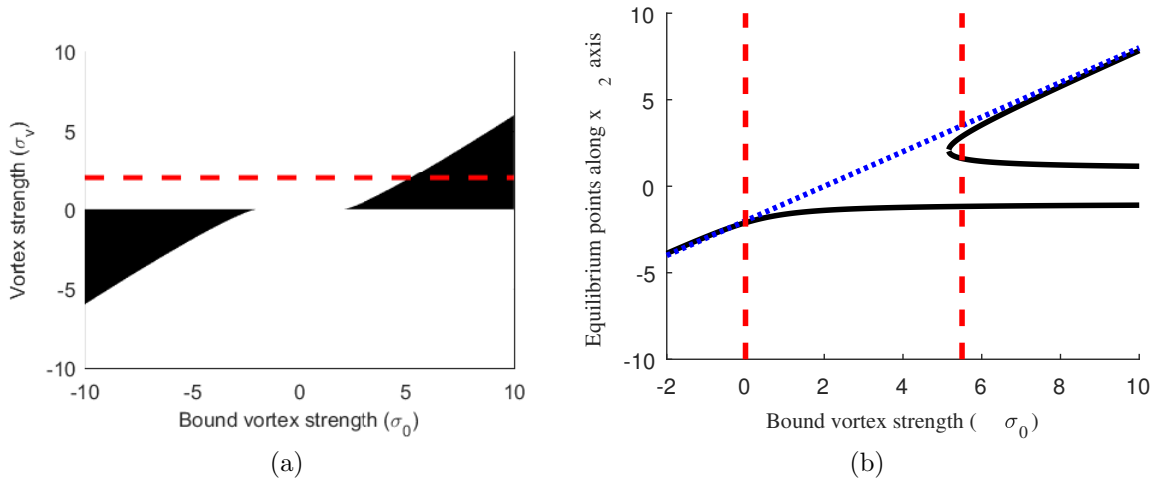


Figure 4.1: a) The black regions show the area in parameter space where the system has three equilibrium points. The dashed line corresponds to the slice shown in Figure 4.1b. b) Bifurcation diagram fixing $\sigma_v = 2$ and varying σ_0 . Equilibrium points far from the cylinder approach the line $\sigma_0 = \sigma_v$, shown as a dotted line.

4.1.2 Closed-Loop Dynamics and bifurcations

In order to design a feedback controller, we linearize (4.2) at any one of the equilibrium points. Let $(\tilde{\mathbf{x}}, \tilde{\mathbf{u}})$ refer to evaluating the derivative at the equilibrium point $x_1 = u_1 = u_2 = 0$, $x_2 = \tilde{x}_2$. We derive the linear system

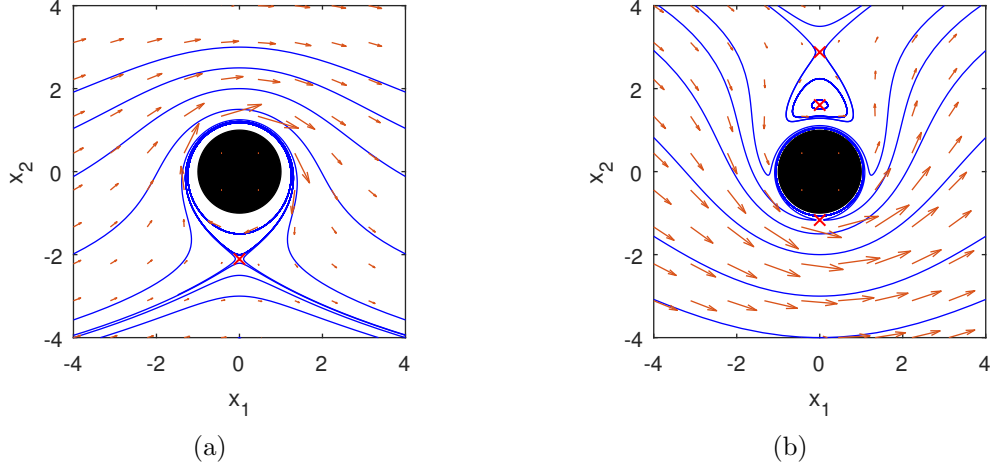


Figure 4.2: Phase portraits for $\sigma_v = 2$. and (a) $\sigma_0 = 0$, (b) $\sigma_0 = 5.5$

$$\begin{bmatrix} \dot{x}_1 \\ \dot{x}_2 \end{bmatrix} = A \begin{bmatrix} x_1 \\ x_2 - \tilde{x}_2 \end{bmatrix} + B \begin{bmatrix} u_1 \\ u_2 \end{bmatrix}, \quad (4.4)$$

where

$$A_{ij} = \left. \frac{\partial \dot{x}_i}{\partial x_j} \right|_{(\tilde{x}, \tilde{u})} \quad \text{and} \quad B_{ij} = \left. \frac{\partial \dot{x}_i}{\partial u_j} \right|_{(\tilde{x}, \tilde{u})}, \quad i, j = 1, 2. \quad (4.5)$$

We have

$$A = \begin{bmatrix} 0 & \frac{\sigma_0}{\tilde{x}_2^2} - \frac{\sigma_v(\tilde{x}_2^2+1)}{(\tilde{x}_2^2-1)^2} - \frac{2}{\tilde{x}_2^3} \\ \frac{\sigma_0}{\tilde{x}_2^2} - \frac{\sigma_v}{(\tilde{x}_2^2-1)} - \frac{2}{\tilde{x}_2^3} & 0 \end{bmatrix} \quad (4.6)$$

and

$$B = \begin{bmatrix} -1 - \frac{1}{\tilde{x}_2^2} & 0 \\ 0 & -1 + \frac{1}{\tilde{x}_2^2} \end{bmatrix}. \quad (4.7)$$

Consider the linear state-feedback control

$$\mathbf{u} = \begin{bmatrix} u_1 \\ u_2 \end{bmatrix} = - \begin{bmatrix} k_{11} & k_{12} \\ k_{21} & k_{22} \end{bmatrix} \begin{bmatrix} x_1 \\ x_2 - \tilde{x}_2 \end{bmatrix} = -K(\mathbf{x} - \tilde{\mathbf{x}}). \quad (4.8)$$

The first subscript in each k indicates which control input the gain corresponds to (1 for surging and 2 for heaving) and the second subscript corresponds to which state it multiplies (x_1 or x_2). We analyze the stability of the feedback system by looking at the eigenvalues of the matrix $A - BK$, as indicated by the trace and determinant. For a 2×2 matrix, the determinant is the product of eigenvalues and the trace is the sum of eigenvalues, so the sign of the determinant and trace can be used to infer the sign of the real part of the eigenvalues and, thus, the stability properties of the system. In particular, a negative determinant implies the equilibrium point is a saddle, i.e., it has one unstable and one stable eigenvalue. If the determinant is positive, then a positive trace indicates the system is unstable and a negative trace indicates the system is exponentially stable, i.e., it is stable and will converge to the equilibrium point [47]. If the determinant is positive and the trace is 0, or if the determinant is 0, then no conclusion can be reached.

Theorem 1. *For an equilibrium point \tilde{x}_2 of (4.2) to be exponentially stable, the following two conditions need to hold:*

$$k_{11}k_{22} - \left(k_{12} + \frac{1}{\tilde{x}_2} - \frac{2\sigma_v\tilde{x}_2^2}{(\tilde{x}_2^2 - 1)^3} \right) \left(k_{21} + \frac{1}{\tilde{x}_2} \right) > 0 \quad (4.9)$$

$$k_{11} + k_{22} + \frac{k_{11} - k_{22}}{\tilde{x}_2^2} > 0. \quad (4.10)$$

Proof. Since (4.10) is the trace of $A - BK$ it must be negative for exponential stability. Condition (4.9) follows from requiring the determinant of $A - BK$ to be positive, i.e.,

$$\det(A - BK) = k_{11}k_{22} \frac{\tilde{x}_2^4 - 1}{\tilde{x}_2^4} - \left(A_{12} + \frac{\tilde{x}_2^2 + 1}{\tilde{x}_2^2} k_{12} \right) \left(A_{21} + \frac{\tilde{x}_2^2 - 1}{\tilde{x}_2^2} k_{21} \right) > 0 \quad (4.11)$$

$$= \left[k_{11}k_{22} - \left(\frac{A_{12}\tilde{x}_2^2}{\tilde{x}_2^2 + 1} + k_{12} \right) \left(\frac{A_{21}\tilde{x}_2^2}{\tilde{x}_2^2 - 1} + k_{21} \right) \right] \frac{\tilde{x}_2^4 - 1}{\tilde{x}_2^4} > 0 \quad (4.12)$$

$$k_{11}k_{22} - \left(\frac{A_{12}\tilde{x}_2^2}{\tilde{x}_2^2 + 1} + k_{12} \right) \left(\frac{A_{21}\tilde{x}_2^2}{\tilde{x}_2^2 - 1} + k_{21} \right) > 0. \quad (4.13)$$

Recall from (4.6),

$$\begin{aligned} A_{21} &= \frac{\sigma_0}{\tilde{x}_2^2} - \frac{\sigma_v}{\tilde{x}_2^2 - 1} - \frac{2}{\tilde{x}_2^3} \\ &= \frac{\sigma_0(\tilde{x}_2^3 - \tilde{x}_2) - \sigma_v\tilde{x}_2^3 - 2(\tilde{x}_2^2 - 1)}{\tilde{x}_2^3(\tilde{x}_2^2 - 1)}. \end{aligned} \quad (4.14)$$

Replace the term $\sigma_v\tilde{x}_2^3$ from rearranging (4.3) as

$$\sigma_v\tilde{x}_2^3 = 1 + \sigma_v(\tilde{x}_2^3 - \tilde{x}_2) - \tilde{x}_2^4. \quad (4.15)$$

The terms with σ_0 cancel, leaving

$$A_{21} = \frac{\tilde{x}_2^4 - 2\tilde{x}_2^2 + 1}{\tilde{x}_2^3(\tilde{x}_2^2 - 1)} = \frac{\tilde{x}_2^2 - 1}{\tilde{x}_2^3}. \quad (4.16)$$

Notice

$$A_{12} = A_{21} - \frac{2\sigma_v}{(\tilde{x}_2^2 - 1)^2}. \quad (4.17)$$

Finally substitute (4.16) and (4.17) into (4.13) to obtain (4.9). □

Theorem 1 applies to any of the possible equilibrium points described in Section 4.1.1. Note that with gains set to 0 and $\tilde{x}_2 < 0$, the corresponding equilibrium point is a saddle, as stated in Section 4.1.1. When feedback is applied, any combination of gains satisfying (4.9) and (4.10) will exponentially stabilize the desired equilibrium point. Note that the conditions (4.9) and (4.10) can be achieved using either k_{11} or k_{22} (diagonal gains) and either k_{12} or k_{21} (cross gains) while setting the other gains to zero. This corresponds to using only surging (i.e., $k_{21} = k_{22} = 0$), only heaving ($k_{11} = k_{12} = 0$), only x_1 feedback ($k_{12} = k_{22} = 0$), or only x_2 feedback ($k_{11} = k_{21} = 0$). These designs may be advantageous if there are limitations with the actuators or with the observers. Additionally, since for each design we have two gains instead of four, it is easier to analyze the effect of each gain.

Corollary 1.1. *For the two-gain designs, i.e., either $k_{11} = 0$ or $k_{22} = 0$ and either $k_{12} = 0$ or $k_{21} = 0$, (4.9) reduces to*

$$k_{12} > k_{1c} > 0 \quad \text{for the lower saddle } (\tilde{x}_2 < 0) \tag{4.18}$$

$$k_{12} < k_{1c} > 0 \quad \text{for the center } (\tilde{x}_2 > 0) \tag{4.19}$$

$$k_{12} < k_{1c} < 0 \quad \text{for the upper saddle } (\tilde{x}_2 > 0) \tag{4.20}$$

or

$$k_{21} > k_{2c} > 0 \quad \text{for the lower saddle } (\tilde{x}_2 < 0) \quad (4.21)$$

$$k_{12} > k_{2c} < 0 \quad \text{for the center } (\tilde{x}_2 > 0) \quad (4.22)$$

$$k_{21} < k_{2c} < 0 \quad \text{for the upper saddle } (\tilde{x}_2 > 0) \quad (4.23)$$

where

$$k_{1c} = \frac{2\sigma_v \tilde{x}_2^2}{(\tilde{x}_2^2 - 1)^3} - \frac{1}{\tilde{x}_2}, \quad k_{2c} = -\frac{1}{\tilde{x}_2}, \quad (4.24)$$

and (4.10) reduces to

$$k_{11} < 0 \quad \text{or} \quad k_{22} < 0. \quad (4.25)$$

Proof. In closed loop with a two-gain design and using the k_{1c} and k_{2c} as defined in (4.24), the stability condition (4.9) can be written as

$$(k_{1c} - k_{12})k_{2c} < 0 \quad \text{or} \quad k_{1c}(k_{2c} - k_{21}) < 0. \quad (4.26)$$

Conditions (4.18) to (4.23) are derived from (4.26) by isolating the corresponding gain and flipping the inequality based on the sign of k_{1c} or k_{2c} for the corresponding equilibrium point. The signs of k_{1c} or k_{2c} are determined from the position and open-loop properties of the equilibrium points. In open-loop, the determinant condition (4.9) is

$$k_{1c}k_{2c} < 0. \quad (4.27)$$

Recall this condition holds for the center and the opposite equality holds for the

saddles. For the lower saddle, $k_{1c} > 0$ and $k_{2c} > 0$, since $\tilde{x}_2 < 0$. For the center and the upper saddle, $k_{2c} < 0$ since $\tilde{x}_2 > 0$. For the center, the product $k_{1c}k_{2c} < 0$, because the equilibrium point is stable and thus $k_{1c} > 0$. Similarly, $k_{1c} < 0$ for the upper saddle, because the product $k_{1c}k_{2c} > 0$. Condition (4.25) follows from (4.10), setting either $k_{11} = 0$ or $k_{22} = 0$, and using the fact that $\tilde{x}_2^2 < 1$. \square

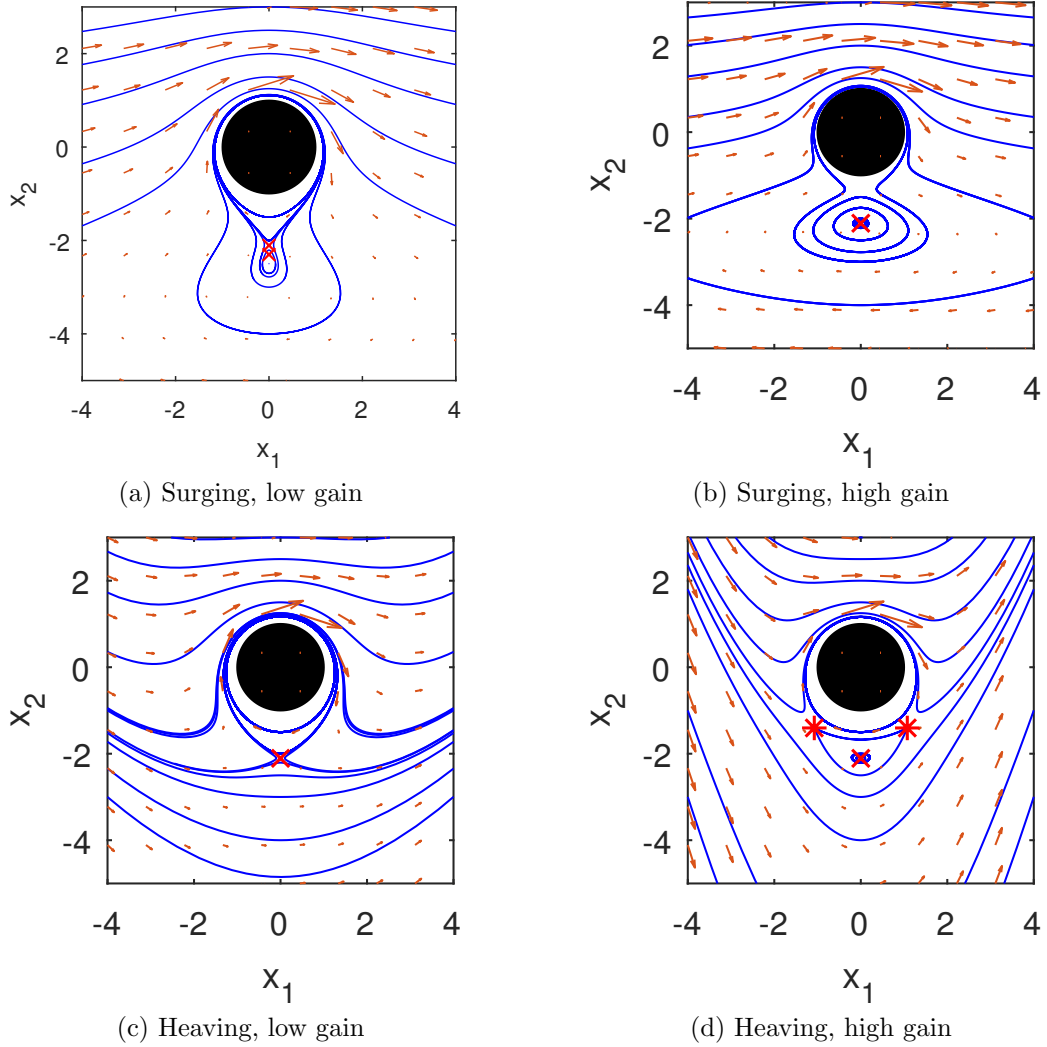


Figure 4.3: Phase planes for the closed-loop system with $\sigma_v = 2, \sigma_0 = 0$, and non-zero cross gains k_{12} (a–b) or k_{21} (c–d). The red X indicates the original equilibrium point, the red dots indicate the new equilibrium points that appear due to feedback. (a) and (c) have gains below conditions (4.18) and (4.21), respectively. (b) and (d) have gains above condition (4.18) and (4.21), respectively.

Several representative cases help to visualize the behavior of the closed-loop system. Fig. 4.3 shows the result of using the cross gains, k_{12} or k_{21} , either 50% below or above their corresponding critical values, with all other gains set to zero. These gains need to satisfy either (4.18) or (4.21), respectively, to convert the lower saddle to a stable node or focus. In Fig. 4.3a, k_{12} (surging) does not satisfy (4.18); the original equilibrium point remains a saddle and a new stable equilibrium point appears below. This new equilibrium point requires a constant surging input, so it is equivalent to stabilizing an equilibrium point at a different nominal freestream velocity. In Fig. 4.3c, the heaving case, no new equilibrium points appear for low values of k_{21} . In Figs. 4.3b and 4.3d, the gains satisfy their critical conditions and, in both cases, the original equilibrium point becomes a center. In the surging case (Fig. 4.3b), a saddle appears between the original equilibrium point and the cylinder, and trajectories near the original equilibrium point form clockwise periodic orbits. In the heaving case (Fig. 4.3b), two saddles appear and orbits near the original equilibrium point are counter-clockwise. From a physical perspective, the two new saddles that appear when choosing k_{21} to satisfy (4.21) can be interpreted as equilibrium points for a different angle of the nominal freestream. Note that even with a gain that satisfies the critical condition, (4.18) or (4.21), trajectories don't converge to the desired equilibrium point because the trace is zero.

Fig. 4.4 shows the effect of adding a small negative diagonal gain to the systems in Figs. 4.3b and 4.3d to make them exponentially stable. Figs. 4.4a and 4.4c have $k_{11} = -0.2$, and Figs. 4.4b and 4.4d have $k_{22} = -0.2$. The band of closed orbits surrounding the equilibrium point in Figs. 4.3b and 4.3d becomes

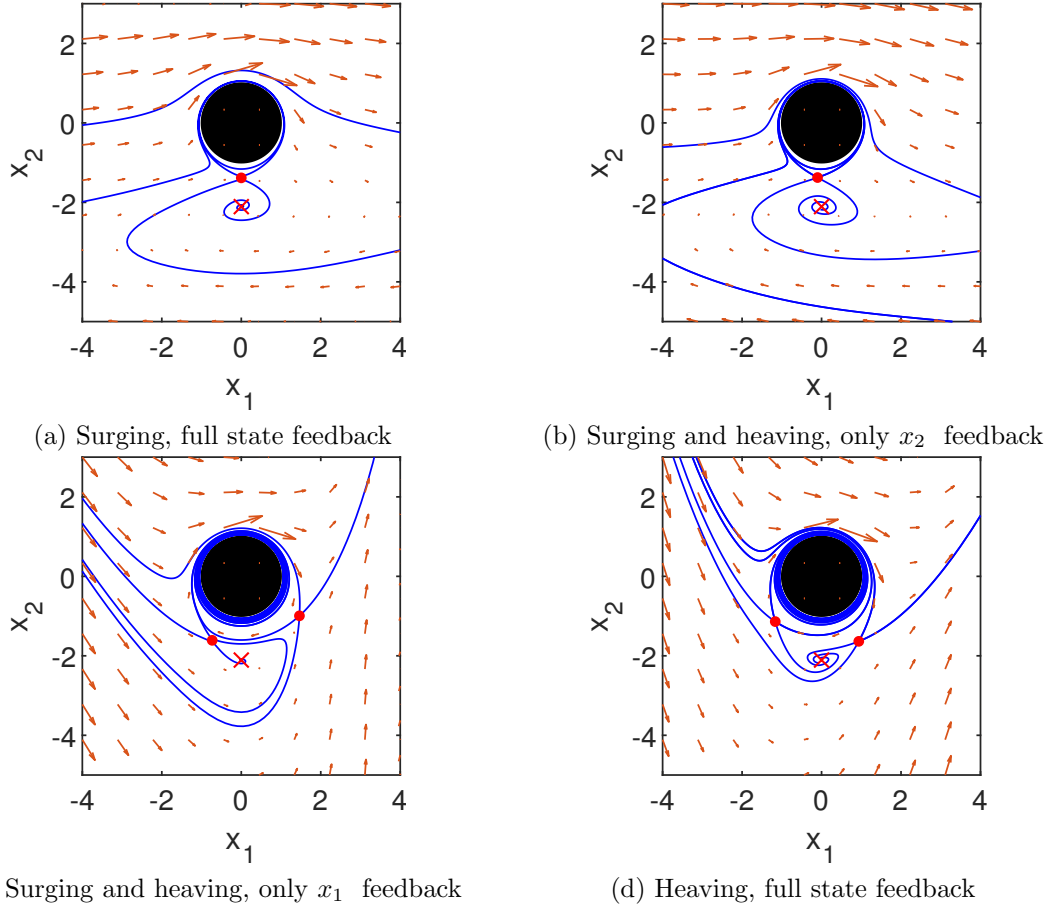


Figure 4.4: Phase planes for the closed-loop with $\sigma_v = 2, \sigma_0 = 0$, and multiple two-gain designs that exponentially stabilize the equilibrium point. The red X indicates the original equilibrium point, the red dots indicate the saddles that appear due to feedback. The trajectories shown approximate the stable and unstable manifolds of the saddles.

a stable spiral that converges to the desired equilibrium point. Since the control design is based on linearization, convergence to the desired equilibrium point is only guaranteed close to the equilibrium point. We estimate the region of attraction by looking at the stable and unstable manifolds of the saddles shown in Fig. 4.4. These orbits separate regions in the phase plane so we can determine whether an orbit will converge by checking if it is in the same region as the stabilized equilibrium point. For the cases shown, using surging and full-state feedback results in the largest

region of attraction.

4.1.3 Summary of results for the cylinder-vortex system

This Section represents a first step in developing a feedback-control framework that stabilizes a vortex near an airfoil using surging and heaving as control input. Conditions on the control gains quantify the requirements to stabilize a vortex near a cylinder and guide the design of more sophisticated nonlinear controllers. The four possible gains in the linear controller are divided into two types, cross and diagonal gains, which correspond to actuation perpendicular and, respectively, parallel to the relative position of the vortex. The original saddle can be exponentially stabilized with a choice of one cross gain and one diagonal gain, while setting others to zero. The cross gains induce a saddle-center bifurcation when above a critical value. After using a cross gain to make the original equilibrium point a center, the diagonal gains exponentially stabilize the desired equilibrium point.

4.2 Dynamics of a Point Vortex Near an Airfoil

4.2.1 Open-Loop Equilibrium points and dynamics

The equilibrium points are found numerically by finding the minimum in the magnitude of the vector derivative. The equilibrium points at low vorticities are hard to obtain because they lie close to the airfoil, where the derivatives blow up. This system was studied in [38], which obtained the equilibrium points using a different method. Figure 4.5 compares the results in [38] with the equilibrium points found in

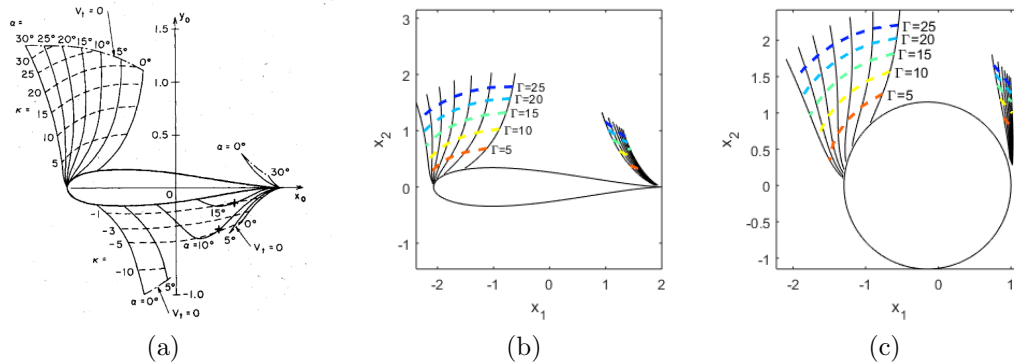


Figure 4.5: Equilibrium points for a vortex near an airfoil in (a) [38] (b) airfoil plane, (c) cylinder plane.

the current implementation. Figure 4.6 shows the corresponding equilibrium points when the system is expressed in the circle plane so that it may be more easily compared to the results of Section 4.1.

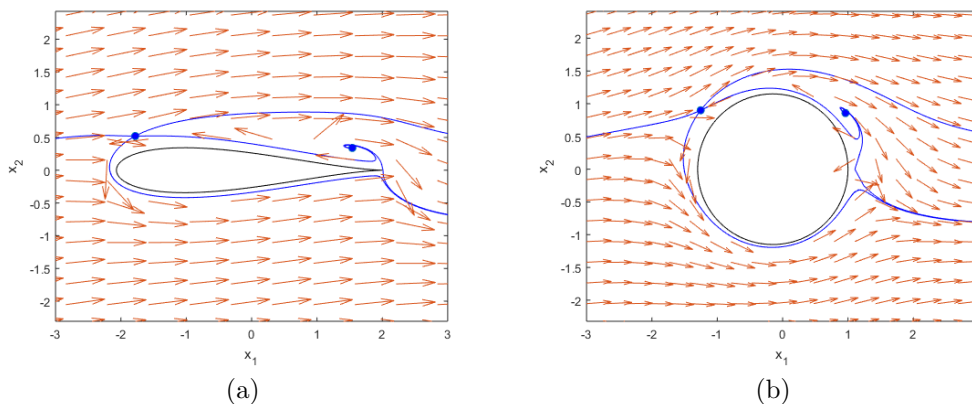


Figure 4.6: Phase portrait for a vortex of strength $\Gamma_v = -5$ near an airfoil at an angle of attack of 10° in the a) airfoil plane b) circle plane. Arrows indicate only direction, not magnitude.

Figure 4.6 shows the phase portrait for the system for a vortex strength of $\Gamma_v = -5$. The blue points indicate the equilibrium points. The equilibrium point near the leading edge is a saddle; the equilibrium point near the trailing edge is an unstable node. Blue lines indicate approximate separatrices. The plane can be

divided into three regions: above and below the airfoil, the trajectory of the airfoil approximates the freestream; very close to the airfoil, the trajectories wrap around the body but don't form a periodic orbit; a small distance above the airfoil, vortices move from the trailing edge to the leading edge, then back and away from the body.

4.2.2 Closed-Loop Dynamics for a vortex near an airfoil

Similarly to the procedure described in 4.1.2, the leading edge equilibrium point can be stabilized using a linear feedback control law of the form

$$\mathbf{u} = \begin{bmatrix} u_1 \\ u_2 \end{bmatrix} = - \begin{bmatrix} k_{11} & k_{12} \\ k_{21} & k_{22} \end{bmatrix} \begin{bmatrix} x_1 - \tilde{x}_1 \\ x_2 - \tilde{x}_2 \end{bmatrix} = -K(\mathbf{x} - \tilde{\mathbf{x}}). \quad (4.28)$$

Where u_1, u_2 correspond to surging and heaving, respectively, and $(\tilde{x}_1, \tilde{x}_2)$ is the leading edge equilibrium point. Unlike the case for the cylinder, here the equilibrium points, Jacobian, and control gains are found numerically. The Jacobian is obtained by applying finite differences at the equilibrium point. The feedback gains that stabilize the equilibrium point are determined by solving for a linear quadratic regulator [48]. Figure 4.7 shows the resulting closed-loop phase portrait in the airfoil plane and the circle plane. The trajectories shown help visualize the region of attraction for this control law. Vortices starting to the left of the trajectories that divide the plane vertically will converge to the desired equilibrium point.

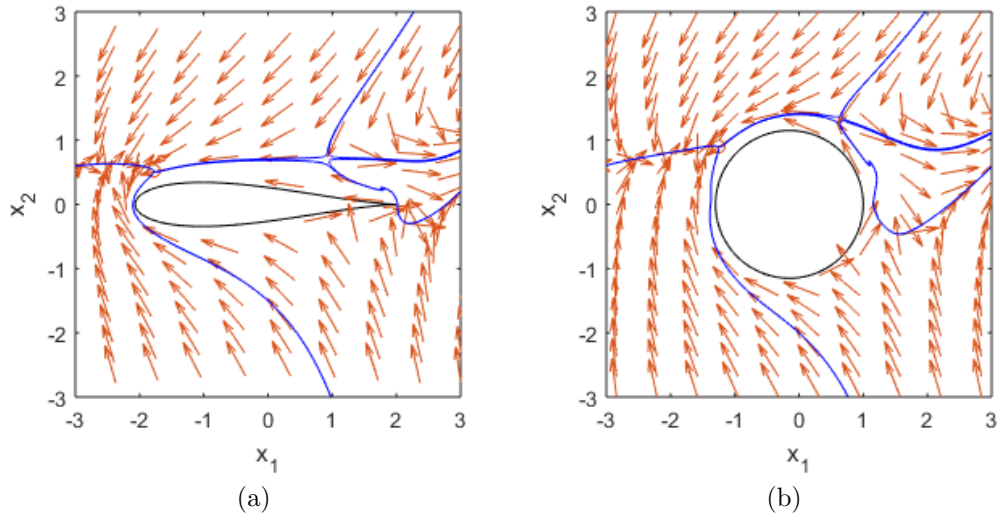


Figure 4.7: Phase portrait for a vortex of strength $\Gamma = -5$ near an airfoil at an angle of attack of 10° with closed loop control in the a) airfoil plane b) circle plane. Arrows indicate only direction, not magnitude.

4.2.3 Summary of results for the airfoil-vortex system

This Section shows preliminary results in extending the model to an airfoil. Due to added mathematical complexity, analytical results could not be obtained, but simulations highlight the differences between both systems. The airfoil-vortex system has two equilibrium points whose position depend on the strength of the free vortex and the angle of attack of the airfoil. The equilibrium points found match the previous literature. Unlike the cylinder-vortex system, no periodic orbits were found. The leading edge vortex is stabilized using linear quadratic regulation.

Chapter 5: Conclusion

5.1 Summary of Contributions

This work has produced two separate results in the sides of estimation and regularization for feedback control of a leading edge vortex. The method for estimation relies on extracting a linear model that approximates the evolution of a high dimensional system using Dynamic Mode Decomposition. A Kalman filter is implemented on this linear model to estimate the state of the flowfield using pressure measurements. This method requires a training step in which both flowfield and pressure measurements are available. The estimate obtained is able to successfully reproduce the flow structures in the flow when the test data is similar to the training data.

The estimate produces a description in terms of the flow velocity at every gridpoint in a region near the airfoil. This is suitable for providing a visual representation of the flow and can highlight what regions are reproduced adequately.

The strategy for control consists of analyzing two 2 dimensional non-linear system which are minimalist representations of the dynamics of a leading edge vortex; a vortex in the presence of an actuated cylinder and airfoil. Conditions on feedback gains that stabilize this system are found analytically for the cylinder case. Equi-

librium points and stabilizing feedback gains are found numerically for the airfoil case. These systems ignore many aspects of the dynamics of a leading edge vortex, but continuing adding details to the model may yield hindsight into the stability properties of the vortex.

5.2 Suggestions for Ongoing and Future Work

To use the DMD-KF for feedback control it is necessary to extract useful information such lift or the position of the leading edge vortex from the flow data. The error measure presented in this paper is defined by comparing the velocity at every grid point, which does not necessarily reflect the quality of the estimation of specific flow features that may needed in practice for an effective feedback control. An important next step is to evaluate the performance of the estimator in terms of the variables that are used for control.

Another topic for future study is the robustness of the DMD-KF by using various actuation profiles and flow conditions. It is unlikely the current approach would work for a wide range of parameters due to the nonlinearities of the system. A possible solution is to train several DMD-KFs with different parameters and run them in parallel. Another alternative to deal with nonlinearities is to use a rich dictionary of observables as in Extended Dynamic Mode Decomposition to better approximate the Koopman modes of the underlying dynamics.

The vortex model in this paper is an abstract representation of the dynamics of a leading edge vortex. Future work should extend the model to account for more

elements relevant to the physics of a leading edge vortex. Additionally, the control strategies developed with these simple systems can be tested in more accurate flow models, such as a point vortex or CFD model.

Bibliography

- [1] C. W. Pitt Ford and H. Babinsky. Lift and the leading-edge vortex. *Journal of Fluid Mechanics*, 720:280–313, 2013.
- [2] Jeff D Eldredge and Anya R Jones. Annual Review of Fluid Mechanics Leading-Edge Vortices : Mechanics and Modeling. 2019.
- [3] Sathesh Mariappan, A. D. Gardner, Kai Richter, and Markus Raffel. Analysis of dynamic stall using Dynamic Mode Decomposition technique. *AIAA Journal*, 52(11):2427–2439, 2014.
- [4] Charles Ellington, Coen van den Berg, Sandy Willmott, and Adrian Thomas. Leading-edge vortices in insect flight. *Nature*, 384:626–630, 12 1996.
- [5] John Kim and Thomas R. Bewley. A Linear Systems Approach to Flow Control. *Annual Review of Fluid Mechanics*, 39(1):383–417, 2007.
- [6] M. Goman and A. Khrabrov. State-space representation of aerodynamic characteristics of an aircraft at high angles of attack. *Journal of Aircraft*, 31(5):1109–1115, 1994.
- [7] Clarence W. Rowley and Scott T.M. Dawson. Model Reduction for Flow Analysis and Control. *Annual Review of Fluid Mechanics*, 49(1):387–417, 2017.
- [8] Kunihiko Taira, Steven L. Brunton, Scott T. M. Dawson, Clarence W. Rowley, Tim Colonius, Beverley J. McKeon, Oliver T. Schmidt, Stanislav Gordeyev, Vassilios Theofilis, and Lawrence S. Ukeiley. Modal analysis of fluid flows: An overview. *AIAA Journal*, 55(12):4013–4041, 2017.
- [9] Aaron Towne, Oliver T. Schmidt, and Tim Colonius. Spectral proper orthogonal decomposition and its relationship to dynamic mode decomposition and resolvent analysis. *Journal of Fluid Mechanics*, 847:821–867, 2018.
- [10] C W Rowley. Model reduction for fluids, using Balanced Proper Orthogonal Decomposition. *International Journal of Bifurcations and Chaos*, 15(3):997–1013, 2005.

- [11] S. Ahuja and C. W. Rowley. Feedback control of unstable steady states of flow past a flat plate using reduced-order estimators. *Journal of Fluid Mechanics*, 645, 2010.
- [12] Peter J. Schmid. Dynamic mode decomposition of numerical and experimental data. *Journal of Fluid Mechanics*, 656(July 2010):5–28, 2010.
- [13] Amit Surana and Andrzej Banaszuk. Linear observer synthesis for non-linear systems using Koopman Operator framework. *IFAC-PapersOnLine*, 49(18):716–723, 2016.
- [14] Field Manar. *Measurements and modeling of the unsteady flow around a thin wing*. PhD thesis, University of Maryland, 2018.
- [15] James Kadtko, Áron Péntek, and Gianni Pedrizzetti. Controlled capture of a continuous vorticity distribution. *Physics Letters A*, 204(2):108–114, aug 1995.
- [16] Taku Nonomura, Hisaichi Shibata, and Ryoji Takaki. Dynamic mode decomposition using a kalman filter for parameter estimation. *AIP Advances*, 8(10):105106, 2018.
- [17] Taku Nonomura, Hisaichi Shibata, and Ryoji Takaki. Extended-kalman-filter-based dynamic mode decomposition for simultaneous system identification and denoising. *PLOS ONE*, 14(2):1–46, 02 2019.
- [18] Matthew O. Williams, Ioannis G. Kevrekidis, and Clarence W. Rowley. A data-driven approximation of the Koopman Operator: extending Dynamic Mode Decomposition. *Journal of Nonlinear Science*, 25(6):1307–1346, dec 2015.
- [19] Maziar S. Hemati, Clarence W. Rowley, Eric A. Deem, and Louis N. Cattafesta. De-biasing the dynamic mode decomposition for applied koopman spectral analysis of noisy datasets. *Theoretical and Computational Fluid Dynamics*, 31(4):349–368, Aug 2017.
- [20] Scott T M Dawson, Maziar S Hemati, Matthew O Williams, and Clarence W Rowley. Characterizing and correcting for the effect of sensor noise in the dynamic mode decomposition. *Experiments in Fluids*, 57(3):1–19, 2016.
- [21] Mihailo R. Jovanović, Peter J. Schmid, and Joseph W. Nichols. Sparsity-promoting Dynamic Mode Decomposition. *Physics of Fluids*, 26(2):1–22, 2014.
- [22] Maziar Hemati, Eric Deem, Matthew Williams, Clarence W. Rowley, and Louis N. Cattafesta. Improving separation control with noise-robust variants of dynamic mode decomposition. 54th AIAA Aerospace Sciences Meeting, 2016.
- [23] Scott T M Dawson, Nicole K Schiavone, Clarence W Rowley, and David R Williams. A Data-Driven Modeling Framework for Predicting Forces and Pressures on a Rapidly Pitching Airfoil. 45th AIAA Fluid Dynamics Conference, 2015.

- [24] Eric Deem, Louis Cattafesta, Huaijin Yao, Maziar Hemati, Hao Zhang, and Clarence W. Rowley. Experimental implementation of modal approaches for autonomous reattachment of separated flows. volume 1052. AIAA Aerospace Sciences Meeting, 01 2018.
- [25] Vernon J. Rossow. Two-fence concept for efficient trapping of vortices on airfoils. *Journal of Aircraft*, 29(5):847–855, sep 1992.
- [26] S. I. Chernyshenko. Stabilization of trapped vortices by alternating blowing suction. *Physics of Fluids*, 7(4):802–807, 1995.
- [27] D. Lentink and M. H. Dickinson. Rotational accelerations stabilize leading edge vortices on revolving fly wings. *Journal of Experimental Biology*, 212(16):2705–2719, 2009.
- [28] Symmetry Reduction and Control of the Dynamics of a 2D Rigid Circular Cylinder and a Point Vortex: Vortex Capture and Scattering. *European Journal of Control*, 13(6):641–655, jan 2007.
- [29] James B. Kadtke and Evgeny A. Novikov. Chaotic capture of vortices by a moving body. I. The single point vortex case. *Chaos (Woodbury, N.Y.)*, 3(4):543–553, 1993.
- [30] Daniel F. Gomez, Francis Lagor, Phillip B. Kirk, Andrew Lind, Anya R. Jones, and Derek A. Paley. Unsteady dmd-based flow field estimation from embedded pressure sensors in an actuated airfoil. AIAA Scitech 2019 Forum.
- [31] Daniel F. Gomez, Francis D. Lagor, Phillip B. Kirk, Andrew H. Lind, Anya R. Jones, and Derek A. Paley. Data-driven estimation of the unsteady flowfield near an actuated airfoil. *Journal of Guidance, Control, and Dynamics*, 2019.
- [32] Daniel F. Gomez and Derek A. Paley. Closed-loop control of the position of a single vortex relative to an actuated cylinder. American Control Conference, 2019.
- [33] Joseph Katz and Allen Plotkin. *Low-Speed Aerodynamics*. Cambridge University Press, Cambridge, 2001.
- [34] L.M. Milne-Thomson. *Theoretical Hydrodynamics*. Dover Books on Physics. Dover Publications.
- [35] Johan Roenby. *Chaos and integrability in ideal body-fluid interactions*. PhD thesis, Technical University of Denmark, 2011.
- [36] J.D. Anderson. *Fundamentals of Aerodynamics*. McGraw-Hill Education, 2010.
- [37] R. R. Clements. An inviscid model of two-dimensional vortex shedding. *Journal of Fluid Mechanics*, 57(2):321–336, 1973.

- [38] M.-K. HUANG and C.-Y. CHOW. Trapping of a free vortex by joukowski airfoils. *AIAA Journal*, 20(3):292–298, 1982.
- [39] Kevin K. Chen, Jonathan H. Tu, and Clarence W. Rowley. Variants of dynamic mode decomposition: Boundary condition, koopman, and fourier analyses. *Journal of Nonlinear Science*, 22(6):887–915, Dec 2012.
- [40] J Nathan Kutz, Steven Brunton, Bingni Brunton, and Joshua L. Proctor. *Dynamic Mode Decomposition: Data-Driven Modeling of Complex Systems*. SIAM, 11 2016.
- [41] John L. Crassidis and John L. Junkins. *Optimal Estimation of Dynamic Systems, Second Edition (Chapman & Hall/CRC Applied Mathematics & Nonlinear Science)*. Chapman & Hall/CRC, 2nd edition, 2011.
- [42] Jonathan H. Tu, Clarence Rowley, Dirk Luchtenburg, Steven Brunton, and J Nathan Kutz. On dynamic mode decomposition: Theory and applications. *Journal of Computational Dynamics*, 1, 11 2013.
- [43] Clarence W. Rowley, Igor Mezi, Shervin Bagheri, Philipp Schlatter, and Dan S. Henningson. Spectral analysis of nonlinear flows. *Journal of Fluid Mechanics*, 641:115–127, 2009.
- [44] Igor Mezić. Analysis of Fluid Flows via Spectral Properties of the Koopman Operator. *Annual Review of Fluid Mechanics*, 45(1):357–378, 2013.
- [45] A. H. Lind. *An Experimental Study of Static and Oscillating Rotor Blade Sections in Reverse Flow*. PhD thesis, University of Maryland, 2015.
- [46] Philip B. Kirk and Anya R. Jones. Vortex formation on surging aerofoils with application to reverse flow modelling. *Journal of Fluid Mechanics*, 859:59–88, 2019.
- [47] S.H. Strogatz. *Nonlinear Dynamics And Chaos*. Studies in nonlinearity. Sarat Book House, 2007.
- [48] Sigurd Skogestad and Ian Postlethwaite. *Multivariable Feedback Control: Analysis and Design*. John Wiley & Sons, Inc., USA, 2005.